NUCLEOSYNTHESIS IN ONeMg NOVAE: MODELS VERSUS OBSERVATIONS TO CONSTRAIN THE MASSES OF ONeMg WHITE DWARFS AND THEIR ENVELOPES

SHINYA WANAJO

Division of Theoretical Astrophysics, National Astronomical Observatory, 2-21-1 Osawa, Mitaka, Tokyo 181-8588, Japan; shinya.wanajo@nao.ac.jp

MASA-AKI HASHIMOTO

Department of Physics, Faculty of Science, Kyushu University, 4-2-1 Ropponmatsu, Tyuo-ku, Fukuoka 810-8560, Japan; hashi@gemini.rc.kyushu-u.ac.jp

AND

KEN'ICHI NOMOTO

Department of Astronomy and Research Center for Early Universe, School of Science, University of Tokyo, 7-3-1 Hongo, Bunkyo-ku, Tokyo 113-0033, Japan; nomoto@astron.s.u-tokyo.ac.jp

ABSTRACT

Nucleosynthesis in ONeMg novae has been investigated with the wide ranges of three parameters, i.e., the white dwarf mass, the envelope mass at ignition, and the initial composition. A quasi-analytic one-zone approach is used with an up-to-date nuclear reaction network. The nucleosynthesis results show correlation with the peak temperatures or the cooling timescales during outbursts. Among the combinations of white dwarf and envelope masses that give the same peak temperature, the explosion is more violent for a lower white dwarf mass owing to its smaller gravitational potential. Comparison of the nucleosynthesis results with observations implies that at least two-thirds of the white dwarf masses for the observed ONeMg novae are $\simeq 1.1 \, M_{\odot}$, which is significantly lower than estimated by previous hydrodynamic studies but consistent with the observations of V1974 Cyg. Moreover, the envelope masses derived from the comparison are $\gtrsim 10^{-4} \, M_{\odot}$, which is in good agreement with the ejecta masses estimated from observations but significantly higher than in previous hydrodynamic studies. With such a low-mass white dwarf and a high-mass envelope, a nova can produce interesting amounts of the γ-ray emitters ^{7}Be, ^{22}Na, and ^{26}Al. We suggest that V1974 Cyg has produced ^{22}Na as high as the upper limit derived from the COMPTEL survey. In addition, a nonnegligible part, if not the majority, of the Galactic ^{26}Al may originate from ONeMg novae. Both the future *International Gamma-Ray Astrophysical Laboratory* (*INTEGRAL*) survey for these γ-ray emitters and abundance estimates derived from ultraviolet, optical, and near-infrared spectroscopy will impose severe constraints on the current nova models.

Subject headings: novae, cataclysmic variables — nuclear reactions, nucleosynthesis, abundances — white dwarfs

1. INTRODUCTION

A classical nova has been thought to be a thermonuclear runaway of hydrogen-rich gas accumulated onto a white dwarf in a close binary system (Truran 1982; Gehrz et al. 1998, and references therein). Recent observations show that about 30% of well-studied events are classified as oxygen-neon-magnesium (ONeMg) novae. Observationally, ONeMg novae are characterized by strong line emission in neon and other intermediate-mass elements such as magnesium, aluminum, silicon, and sulfur in their ejected shells (Livio & Truran 1994). The presence of these elements implies that the accumulated gases must have been substantially enriched through the dredge-up from the ONeMg cores.

ONeMg novae have been suggested to be a promising production site of the γ-ray emitters ^{7}Be, ^{22}Na, and ^{26}Al (Starrfield, Truran, & Sparks 1978; Weiss & Truran 1990; Nofar, Shaviv, & Starrfield 1991; Starrfield et al. 1993, 1998; Coc et al. 1995; Politano et al. 1995; Hernanz et al. 1996; Wanajo et al. 1997a, 1997b; José, Hernanz, & Coc 1997; José & Hernanz 1998). However, the following three uncertainties confront us when studying nucleosynthesis in ONeMg novae. First, the mass of the ONeMg white dwarf is not constrained from theoretical models any more than ~ 1.1–$1.4 \, M_{\odot}$, which results from the 8–10 $M_{\odot}$ stellar evolution models (Nomoto 1984, 1987; Iben & Tutukov 1985).

On the other hand, only a few observational estimates of the white dwarf masses have been reported (Paresce et al. 1995; Krautter et al. 1996; Retter, Leibowitz, & Ofek 1997). Second, there is a serious disagreement between observational estimates and current theories on the masses accreted onto white dwarfs. The ONeMg white dwarfs in previous hydrodynamic studies accumulate a few times $10^{-5} \, M_{\odot}$ of the envelope masses at ignition (Politano et al. 1995; Starrfield et al. 1998; José & Hernanz 1998). On the other hand, the estimated ejecta masses of QU Vul, V838 Her, and V1974 Cyg are $\sim 10^{-4}$–$10^{-3} \, M_{\odot}$ (Taylor et al. 1987; Greenhouse et al. 1988; Saizar et al. 1992, 1996; Woodward et al. 1992, 1997; Pavelin et al. 1993; Shore et al. 1993; Vanlandingham et al. 1996), which is 10–100 times larger than theoretical estimates. Starrfield et al. (1998) have shown that the envelope mass increases with decreasing mass accretion rate and white dwarf luminosity (see also Prialnik & Kovetz 1995; Kovetz & Prialnik 1997). However, it is still significantly lower than observational estimates. Third, there has been no consensus on the mixing mechanism between the white dwarf matter and the accreted gas, though a few hypotheses such as diffusion, shear mixing, and convective overshooting have been proposed (Prialnik & Kovetz 1984; Kutter & Sparks 1987; Iben, Fujimoto, & MacDonald 1991; Glasner, Livne, & Truran 1997; Kercek, Hillebrandt, & Truran 1998a, 1998b). Furthermore,

the metallicity estimates for the observed ejecta of ONeMg novae show a wide spread between 0.09 and 0.86 in mass fraction (Livio & Truran 1994; Politano et al. 1995; Starrfield et al. 1998). The initial composition of an envelope may significantly affect the nucleosynthesis result as well as the energetics of the outburst (Kovetz & Prialnik 1997; José & Hernanz 1998).

The purpose of this study is to examine nucleosynthesis in ONeMg novae with the wide ranges of three parameters: the white dwarf mass, the envelope mass, and the mixing ratio of the core-surface matter into the envelope. In § 2, we describe our quasi-analytic nova models and an updated nuclear reaction network. We then, in § 3, compare the nucleosynthesis results for one sequence with a previous hydrodynamic calculation. In § 4, we constrain the ranges of white dwarf and envelope masses, comparing the nucleosynthesis results with observational abundance estimates in which the effect of changing the initial composition is considered. Finally, the γ-ray line emissions from ^{7}Be, ^{22}Na, and ^{26}Al are discussed in § 6.

2. METHOD OF CALCULATION

2.1. Nova Model

Our nova models are based on the quasi-analytic approach for the hydrogen shell flash on a white dwarf (Sugimoto & Fujimoto 1978; Fujimoto 1982a, 1982b). The temperature and density structures of an envelope are obtained analytically for a given set of a white dwarf mass (M_{WD}) and an envelope mass (M_{env}), on the assumption that the spherical envelope expands in hydrostatic equilibrium. We have constructed models for 49 sets of M_{WD} (1.05–1.35 $M_\odot$) and M_{env} (10^{-6} to 10^{-3} $M_\odot$). The former corresponds to the masses of ONeMg cores that result from 8–10 $M_\odot$ stellar evolutions (Nomoto 1984, 1987; Iben & Tutukov 1985), and the latter covers those both from theories ($\sim 10^{-5}$ to 10^{-4} $M_\odot$; Truran et al. 1977; Politano et al. 1995; Starrfield et al. 1998; José & Hernanz 1998) and from observations ($\gtrsim 10^{-4}$ $M_\odot$; Taylor et al. 1987; Greenhouse et al. 1988; Saizar et al. 1992, 1996; Woodward et al. 1992, 1997; Pavelin et al. 1993; Shore et al. 1993; Vanlandingham et al. 1996). The filled circles in Figure 1 are the sequences at which our numerical calculations are performed, while squares, triangles, and stars are taken from hydrodynamic studies by Politano et al. (1995, hereafter PSTWS95), Starrfield et al. (1998, hereafter STWS98), and José & Hernanz (1998, hereafter JH98), respectively. The solid lines show the mass accretion rates onto the white dwarfs required for each set of (M_{WD}, M_{env}) calculated by Fujimoto (1982b). These are in reasonable agreement with those by PSTWS95, STWS98, and JH98 ($\sim 10^{-10}$ to 10^{-9} $M_\odot$ yr^{-1}), but are somewhat overestimated in Fujimoto (1982b) since the luminosities of white dwarfs are neglected and the radii are assumed to be Chandrasekhar (see Fig. 3) in his work. Note that no outburst is achievable by an accreting white dwarf below the dashed line because of the high accretion rate. It is obvious that a rather low accretion rate (or a low luminosity of the white dwarf) is required to obtain a massive envelope such as $\gtrsim 10^{-4}$ to 10^{-3} $M_\odot$, as expected from observations.

The quasi-analytic nova model has been elaborated by Sugimoto & Fujimoto (1978) and Fujimoto (1982a, 1982b). Let us discuss the model in some detail, since it can characterize the nova burst very well. The pressure and the density
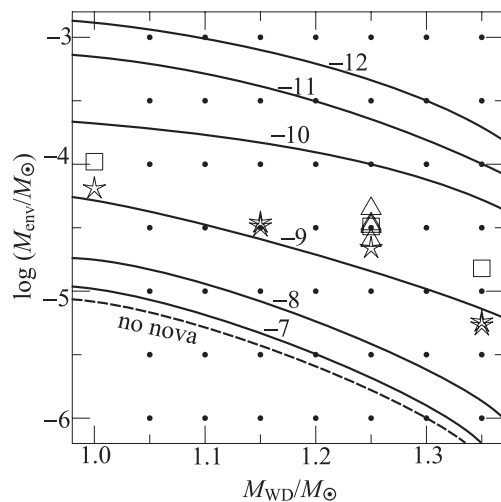

FIG. 1.—(M_{WD}, M_{env}) sequences at which our numerical calculations have been carried out. The dots denote this work, and squares, triangles, and stars are, respectively, from Politano et al. (1995), Starrfield et al. (1998), and José & Hernanz (1998).

at the base of the envelope are expressed in terms of M_{WD} and M_{env}:

$$P_b = \frac{GM_{WD}M_{env}}{4\pi R_{WD}^4} f_b , \tag{1}$$

$$\rho_b = \frac{M_{env}}{4\pi R_{WD}^3} V_b f_b , \tag{2}$$

where R_{WD} is the radius of the white dwarf and V is a homologous invariant defined by

$$V \equiv -\frac{d\ln P}{d\ln r} = \frac{GM\rho}{rP} .$$

Hereafter the subscript b denotes a quantity at the base of the envelope. The flatness parameter f in equations (1) and (2) decreases monotonically as the shell flash proceeds:

$$f(x, N) \equiv \frac{x^{N+1}(1-x)^{3-N}}{(N+1)B_x(N+1, 3-N)} , \tag{3}$$

where

$$x \equiv \frac{N+1}{V} \quad (0 < x < 1) . \tag{4}$$

The value of f_b denotes the degree of the "flatness" of the envelope. For $f_b \sim 1$ ($x_b \sim 0$), the envelope is thin and strongly degenerate and thus is flat. On the other hand, for $f_b \sim 0$ ($x_b \sim 1$), the envelope is thick and nondegenerate and thus is spherical. The polytropic index N in equations (3) and (4) is defined by

$$\frac{N}{N+1} \equiv \frac{d\ln \rho}{d\ln P} ,$$

and $B_x(p, q)$ is the incomplete β-function defined by

$$B_x(p, q) \equiv \int_0^x t^{p-1}(1-t)^{q-1} dt \quad (0 < x < 1) .$$

N is assumed to be adiabatic and constant throughout the envelope but varies with time. The effect of the spatial variation in N is quite small for a typical convective envelope (Fujimoto 1982a). The value of N is approximately 1.5 at the beginning of a shell flash, and approaches ~ 3 at the end because of the increasing radiation pressure.

The shell flash starts with $f_b \sim 1$ ($x_b \sim 0$). The envelope is then heated up by nuclear burning to a thermal runaway, and cools down when f_b decreases to ~ 0 ($x_b \sim 1$). Equations (1) and (2) are valid if

$$\theta \equiv \frac{Ux}{1-x} \ll 1 \tag{5}$$

is satisfied, where

$$U \equiv \frac{d\ln M}{d\ln r} = \frac{4\pi r^3 \rho}{M}$$

is another homologous invariant. This condition is violated only near the last phase of the shell flash ($f_b \sim 0$). At this phase, major nuclear reactions are frozen out except for the p-p chain, the CNO cycle, and β^+-decay. Thus, our nucleosynthesis results may not be significantly affected.

Figure 2 illustrates contours for P_b/f_b and $\rho_b/V_b f_b$ in the M_{WD}-M_{env} space. These are the proper quantities for each set of (M_{WD}, M_{env}). The stronger dependence of the former on M_{WD} is due to the higher power of R_{WD} as seen in equations (1) and (2). The temperature at the base of the envelope T_b can be calculated by solving the equation of state with the use of equations (1) and (2). The spatial variations of the pressure, the density, and the temperature are given, when condition (5) is satisfied, by

$$P(x) = P_b \left(\frac{x}{x_b}\right)^{N+1} \left(\frac{1-x}{1-x_b}\right)^{-(N+1)},$$

$$\rho(x) = \rho_b \left(\frac{x}{x_b}\right)^{N} \left(\frac{1-x}{1-x_b}\right)^{-N},$$

$$T(x) = T_b \left(\frac{x}{x_b}\right)^{(N+1)\nabla} \left(\frac{1-x}{1-x_b}\right)^{-(N+1)\nabla},$$

where $\nabla \equiv d\ln T/d\ln P$ is assumed to be adiabatic and constant throughout the envelope but varies with time (on the deviation from constant ∇, see Fujimoto 1982a). The value of x decreases monotonically with increasing radius, approaching zero at the surface of the envelope. The surface radius R is given, when condition (5) is satisfied, by
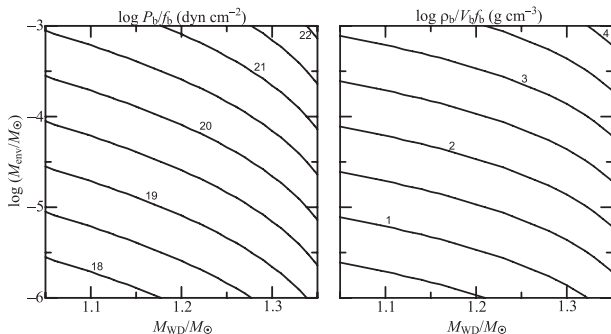
$$R = \frac{R_{WD}}{1-x_b}. \tag{6}$$

Now we know the envelope structure completely.

The progress of a shell flash is derived by energy conservation,

$$\frac{ds}{dt} = \frac{\varepsilon_N}{\langle T \rangle}, \tag{7}$$

where ε_N is the nuclear energy generation rate per unit mass, s is the specific entropy that is spatially constant in the convective envelope, and $\langle T \rangle$ is the mass-averaged temperature over the envelope.

The energy inflow from the white dwarf and loss from the photosphere are neglected, being much smaller than the nuclear energy during the explosive hydrogen burning. The time variation of x_b is then calculated from equations (1), (2), and (7) with the use of the equation of state. The expansion velocity of the envelope v_{exp} is derived from equation (6) as

$$v_{exp} = \frac{R}{1-x_b} \frac{dx_b}{dt}.$$

Each calculation starts with the initial temperature $T_b = 5 \times 10^7$ K and ceases when the nuclear luminosity decreases to the Eddington luminosity, where no further heavy elements are synthesized.

The M_{WD}-R_{WD} relation is derived for an isothermal core (2×10^7 K) consisting of oxygen, neon ($= 5:3$), and partially degenerate electron gases including the effect of the Coulomb interaction (Ichimaru & Kitamura 1994), as shown in Figure 3. The solid line denotes our results and the triangles are taken from PSTWS95 and STWS98. Our results are between those of carbon and magnesium white dwarfs by Hamada & Salpeter (1961) and somewhat smaller than those by PSTWS95 and STWS98. A variation of R_{WD} significantly influences the density due to $\rho_b \propto R_{WD}^{-3}$ as seen in equation (2), much more than the temperature ($\propto R_{WD}^{-1}$). Note that the ONe white dwarf is unable to increase its
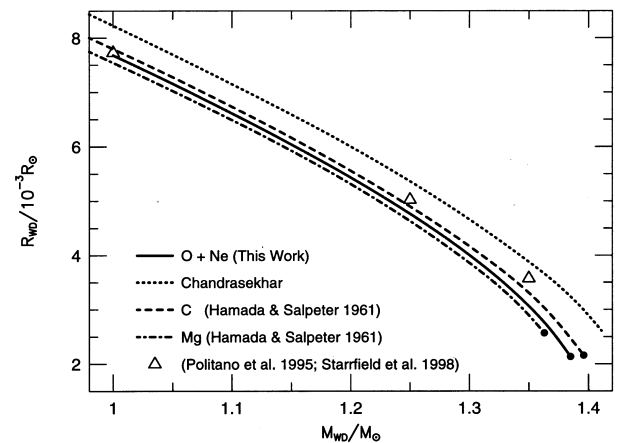
FIG. 3.—M-R relations for various white dwarfs. The solid line is for O:Ne = 5:3 (this work), the dotted line is for the completely degenerate electron gas by Chandrasekhar's method ($Y_e = 0.5$), and the dashed and dot-dashed lines are for carbon and magnesium, respectively (Hamada & Salpeter 1961). The filled circles on the lines for O + Ne, carbon, and magnesium denote values at which neutronization occurs. The triangles are taken from PSTWS95 and STWS98.

FIG. 2.—Contours of the proper values for the pressure (P_b/f_b) and the density ($\rho_b/V_b f_b$) in the logarithmic scale in the M_{WD}-M_{env} space.

TABLE 1

NUCLEAR REACTION NETWORK EMPLOYED

Element	A_{min}	A_{max}	Element	A_{min}	A_{max}
H	1	2	Na	20	23
He......	3	4	Mg......	21	26
Li	7	7	Al	22	27
Be	7	7	Si	24	30
B	8	11	P	27	31
C	9	13	S	28	34
N	13	15	Cl	31	37
O	14	18	Ar.......	32	38
F	17	19	K	35	39
Ne.....	18	22	Ca	36	40

mass beyond 1.38 $M_\odot$ because the electron capture on ^{20}Ne and ^{24}Mg triggers the collapse (denoted by a filled circle on the solid line; Nomoto 1984, 1987).

2.2. *Nuclear Reaction Network and Initial Composition*

The nuclear reaction network used in this work contains 87 stable and proton-rich isotopes from hydrogen to calcium (Table 1), including all relevant nuclear reactions and weak interactions. The reaction ^{8}B(p, γ)^{9}C, which can be a sink for ^{7}Be production (Boffin et al. 1993), is also included. The ground and isomeric states of ^{26}Al take longer than the mean lifetime of the isomer ($\simeq 9.2$ s) to be equilibrated for $\lesssim 4 \times 10^8$ K (Ward & Fowler 1980). The peak temperatures in the models responsible for the observed ONeMg novae may be less than 4×10^8 K, as will be discussed in § 5. Thus, the two states are separated as different isotopes. The nuclear reaction rates are taken from F.-K. Thielemann (1995, private communication). They are based on the rates by Caughlan & Fowler (1988), those calculated by a statistical model (Truran, Thielemann, & Arnould 1987), and the latest experimental data (van Wormer et al. 1994, etc.). We also include new reaction rates by Herndl et al. (1995) and Iliadis et al. (1996). The rate ^{26}Si(p, γ)^{27}P (Herndl et al. 1995) may have a special importance, being 10^3–10^4 times larger than the previous one in the typical nova temperature range. The rates ^{25}Mg(p, γ)^{26}Al and ^{25}Al(p, γ)^{26}Si (Iliadis et al. 1996) may be also of importance for ^{26}Al production, though the latter involves a large uncertainty. In our computations, all nuclear reaction rates are mass averaged over the envelope, except for β^+-decay that does not depend on density and temperature.

The initial composition of an envelope is assumed to be a mixture of the solar composition gas and the dredged-up matter from the surface of the ONeMg white dwarf. The solar abundances are adopted from Anders & Grevesse (1989), and the abundances of the ONeMg core matter from Hashimoto, Iwamoto, & Nomoto (1993) for the 1.35 $M_\odot$ ONeMg core (Table 2). As can be seen in Table 2,

TABLE 2

ABUNDANCES OF THE ONeMg CORE AT THE SURFACE

Nucleus	Mass Fraction	Nucleus	Mass Fraction
^{12}C	3.95E$-$02	^{24}Mg......	4.20E$-$02
^{16}O	5.42E$-$01	^{25}Mg......	6.29E$-$03
^{20}Ne......	3.31E$-$01	^{26}Mg......	4.57E$-$03
^{21}Ne......	2.87E$-$03	^{27}Al	1.25E$-$02
^{22}Ne......	1.34E$-$03	^{28}Si	2.46E$-$03
^{23}Na......	1.65E$-$02		

TABLE 3

INITIAL COMPOSITIONS OF THE ENVELOPE BY MASS

ISOTOPE	X_{WD}		
	0.1	0.4	0.8
p...........	6.36E$-$01	4.24E$-$01	1.41E$-$01
D..........	4.33E$-$05	2.88E$-$05	9.62E$-$06
^{3}He	2.64E$-$05	1.76E$-$05	5.87E$-$06
^{4}He	2.48E$-$01	1.65E$-$01	5.51E$-$02
^{7}Li	8.43E$-$09	5.62E$-$09	1.87E$-$09
^{11}B	4.26E$-$09	2.84E$-$09	9.46E$-$10
^{12}C	6.69E$-$03	1.76E$-$02	3.22E$-$02
^{13}C	3.29E$-$05	2.19E$-$05	7.31E$-$06
^{14}N	9.96E$-$04	6.64E$-$04	2.21E$-$04
^{15}N	3.93E$-$06	2.62E$-$06	8.74E$-$07
^{16}O	6.28E$-$02	2.22E$-$01	4.35E$-$01
^{17}O	3.50E$-$06	2.34E$-$06	7.79E$-$07
^{18}O	1.95E$-$05	1.30E$-$05	4.34E$-$06
^{19}F	3.65E$-$07	2.43E$-$07	8.11E$-$08
^{20}Ne	3.45E$-$02	1.33E$-$01	2.65E$-$01
^{21}Ne	2.90E$-$04	1.15E$-$03	2.29E$-$03
^{22}Ne	2.51E$-$04	6.15E$-$04	1.10E$-$03
^{23}Na	1.68E$-$03	6.60E$-$03	1.32E$-$02
^{24}Mg......	4.66E$-$03	1.71E$-$02	3.37E$-$02
^{25}Mg......	6.89E$-$04	2.55E$-$03	5.04E$-$03
^{26}Mg......	5.27E$-$04	1.88E$-$03	3.67E$-$03
^{27}Al	1.31E$-$03	5.05E$-$03	1.00E$-$02
^{28}Si	8.34E$-$04	1.38E$-$03	2.10E$-$03
^{29}Si	3.09E$-$05	2.06E$-$05	6.86E$-$06
^{30}Si	2.12E$-$05	1.41E$-$05	4.71E$-$06
^{31}P	7.35E$-$06	4.90E$-$06	1.63E$-$06
^{32}S	3.57E$-$04	2.38E$-$04	7.93E$-$05
^{33}S	2.90E$-$06	1.94E$-$06	6.45E$-$07
^{34}S	1.68E$-$05	1.12E$-$05	3.74E$-$06
^{35}Cl	2.28E$-$06	1.52E$-$06	5.07E$-$07
^{37}Cl	7.70E$-$07	5.13E$-$07	1.71E$-$07
^{36}Ar.......	6.98E$-$05	4.65E$-$05	1.55E$-$05
^{38}Ar.......	1.39E$-$05	9.24E$-$06	3.08E$-$06
^{39}K	3.13E$-$06	2.08E$-$06	6.95E$-$07
^{40}Ca	5.40E$-$05	3.60E$-$05	1.20E$-$05

O:Ne:Mg $\approx$ 10:6:1, which is in good agreement with those in Nomoto & Hashimoto (1988) for $M_{WD} = 1.26$, 1.36 $M_\odot$ and Ritossa, García, & Iben (1996) for $M_{WD} = 1.2$ $M_\odot$. This implies that the composition of an ONeMg core does not significantly depend on its mass. The mass fraction of the dredge-up matter from the ONeMg core in the envelope X_{WD}, which is the third parameter in this study, is of importance on the nucleosynthesis results, as will be discussed in § 4.3. However, abundance estimates in the observations of nova ejecta involve large uncertainties, as pointed out by Livio & Truran (1994). The estimated metallicities of the six observed ONeMg nova ejecta range widely (see Table 4), and, unfortunately, different authors have provided different values even for identical events (Williams et al. 1985; Snijders et al. 1987; Saizar et al. 1992, 1996; Andreä, Drechsel, & Starrfield 1994; Austin et al. 1996; Vanlandingham et al. 1996; Vanlandingham, Starrfield, & Shore 1997). In addition, no consensus has been achieved in theoretical modeling of how and when the core matter mixes into the envelope (Prialnik & Kovetz 1984; Iben et al. 1991; Kutter & Sparks 1987; Glasner et al. 1997; Kercek et al. 1998a, 1998b). Thus, we examine all the combinations of (M_{WD}, M_{env}) for $X_{WD} = 0.1$ (case A), 0.4 (case B), and 0.8 (case C), which cover observational uncertainties in abundance

determinations. The initial compositions for each case are given in Table 3.

3. COMPARISON WITH NUCLEOSYNTHESIS BY A HYDRODYNAMIC MODEL

Up to now, a number of works on nucleosynthesis in ONeMg novae have been performed (Hillebrandt & Thielemann 1982; Weiss & Truran 1990; Nofar et al. 1991, and references therein). Their nova models were, however, based on one-zone envelopes, using the spatially constant temperature and density profiles taken from hydrodynamic studies (Starrfield et al. 1978; Starrfield, Sparks, & Shaviv 1988). Coc et al. (1995) have studied ^{22}Na and ^{26}Al production in ONeMg novae with another semianalytic method (MacDonald 1983). Their nova model and ours give similar envelope structures in temperature and density. However, our model includes the effect of the partially degenerate and relativistic electron gas, while Coc et al. (1995) treated electrons as the ideal gas. The electron degeneracy cannot be neglected in the early phase of outbursts. Hernanz et al. (1996) and José et al. (1997) have also examined nucleosynthesis in novae with the use of a hydrodynamic method. However, they focused on ^{7}Li or ^{26}Al production and gave only a few synthesized isotopes in their papers.

Hence, we compare our model with sequence 6 in STWS98 to see the differences of nucleosynthesis between the quasi-analytic and hydrodynamic methods. The nova model in STWS98 was identical to that of PSTWS95, except that the former included the updated nuclear reaction rates (van Wormer et al. 1994; Herndl et al. 1995) and OPAL opacity tables (Iglesias & Rogers 1993). In addition, STWS98 employed a lower white dwarf luminosity and a lower mass accretion rate to obtain a more massive ignition envelope. Furthermore, an important change was that STWS98 used a longer mixing length of 2–3 times the pressure scale height. We do not compare our results with those of JH98, who studied nucleosynthesis in ONeMg (and CO) novae using a hydrodynamic code, since the white dwarf radii are not presented. Their results showed, however, trends similar to those of PSTWS95 and STWS98. To facilitate comparison, we use the same initial composition, nuclear reaction rates, $M_{\rm WD}$ (=1.25 $M_\odot$), $M_{\rm env}$ (=4.5 $\times$ 10^{-5} $M_\odot$), and $R_{\rm WD}$ as STWS98. Note that the nucleosynthesis results in this work are obtained for the whole envelope, while those in STWS98 are for only the ejected matter. Thus, STWS98 may strongly reflect the composition of the outer region. Figure 4 shows the ratios of isotopes (*filled circles*) and elements (*triangles*) between our results and those of STWS98 (sequence 6). Our calculation obtains a higher peak temperature ($\simeq 3.17 \times 10^8$ K) than that of STWS98 ($\simeq 3.00 \times 10^8$ K), since the latter model ignited hydrogen one zone above the base so that the envelope is effectively thinner (see STWS98). The prominent underproduction of several isotopes like ^{15}N, ^{18}O, ^{21}Ne, ^{22}Na (and perhaps ^{23}Na, not shown in STWS98; see PSTWS95, for instance), ^{24}Mg, and ^{26}Mg is due to our assumption of a fully convective one-zone envelope. Since these isotopes are rather fragile against the (p, γ) or (p, α) reactions, they decrease significantly even at the late phase of the outburst. In contrast, these isotopes were able to survive in STWS98, escaping from the hotter convective region into the cooler radiative region at the late phase. ^{15}N is especially fragile against the (p, α) reaction, being under-
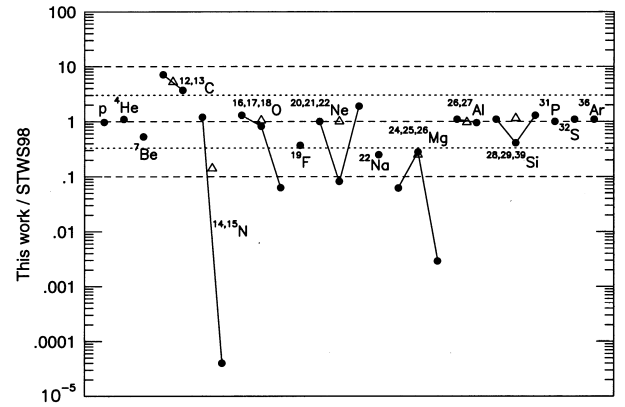

FIG. 4.—Ratios of our nucleosynthesis results to those of STWS98 (sequence 6). The dots and triangles denote isotopes and elements, respectively.

produced by more than 5 orders of magnitude in this work. As a result, nitrogen (mostly ^{14}N in this work) is also underproduced, unlike in STWS98, in which ^{15}N is dominant. On the other hand, carbon (^{12}C and ^{13}C) are significantly overproduced, transferred from ^{15}N. We should be careful on these differences in comparing the nucleosynthesis results with observations. However, both results are in excellent agreement for other isotopes and especially for elements (except for carbon and nitrogen) that are more important for comparison with observations.

4. NUCLEOSYNTHESIS IN ONeMg NOVAE

4.1. *Nuclear Flows in the N-Z Plane*

In this section, we present some important aspects of nucleosynthesis in ONeMg novae, referring to the results of several ($M_{\rm WD}$, $M_{\rm env}$) models. Figure 5 shows the final abundances and the net nuclear flows in the N-Z plane. The size of a circle denotes the mole fraction of the isotope defined by $Y_i \equiv X_i/A_i$ in the logarithmic scale. The initial composition is shown by dotted circles. The net nuclear flow of a reaction from the ith to jth isotope, defined as

$$F_{ij} \equiv \int [\dot{Y}_i(i \rightarrow j) - \dot{Y}_j(j \rightarrow i)]dt \,,$$

is denoted by the length of an arrow in the same scale. Throughout this section, the mixing ratio $X_{\rm WD}$ is assumed to be 0.4 (case B), which is close to the average metallicity of the ejecta estimated from observations (see Z in Table 4).

Figure 6 shows the peak temperature at the base $T_{\rm peak}$, the cooling timescale τ, defined as the duration from the peak to one-half the peak temperature, the peak nuclear energy generation rate per unit mass $\varepsilon_{\rm peak}$, and the ejection velocity $v_{\rm ej}$ in the $M_{\rm WD}$-$M_{\rm env}$ space. Here, $v_{\rm ej}$ is defined as the expansion velocity $v_{\rm exp}$ when it equals the escape velocity $v_{\rm esc}$ (for the models denoted by circles). For the models denoted by crosses, in which $v_{\rm exp}$ is below $v_{\rm esc}$ throughout the calculations, $v_{\rm ej}$ is replaced with $v_{\rm exp}$ at the maximum. As seen in Figure 6, τ has a weaker dependence on $M_{\rm WD}$ than does $T_{\rm peak}$, while the trend of $\varepsilon_{\rm peak}$ is similar to $T_{\rm peak}$. As a result, among the models of the same peak temperature, the explosion is more violent for the smaller $M_{\rm WD}$ because of its smaller gravitational potential. This is also seen in the panel of $v_{\rm ej}$, which shows the similar trend to τ in the $M_{\rm WD}$-$M_{\rm env}$ space. In order to obtain the fast ejection velocities, such as $\gtrsim 1000$ km s^{-1} as derived by recent observations

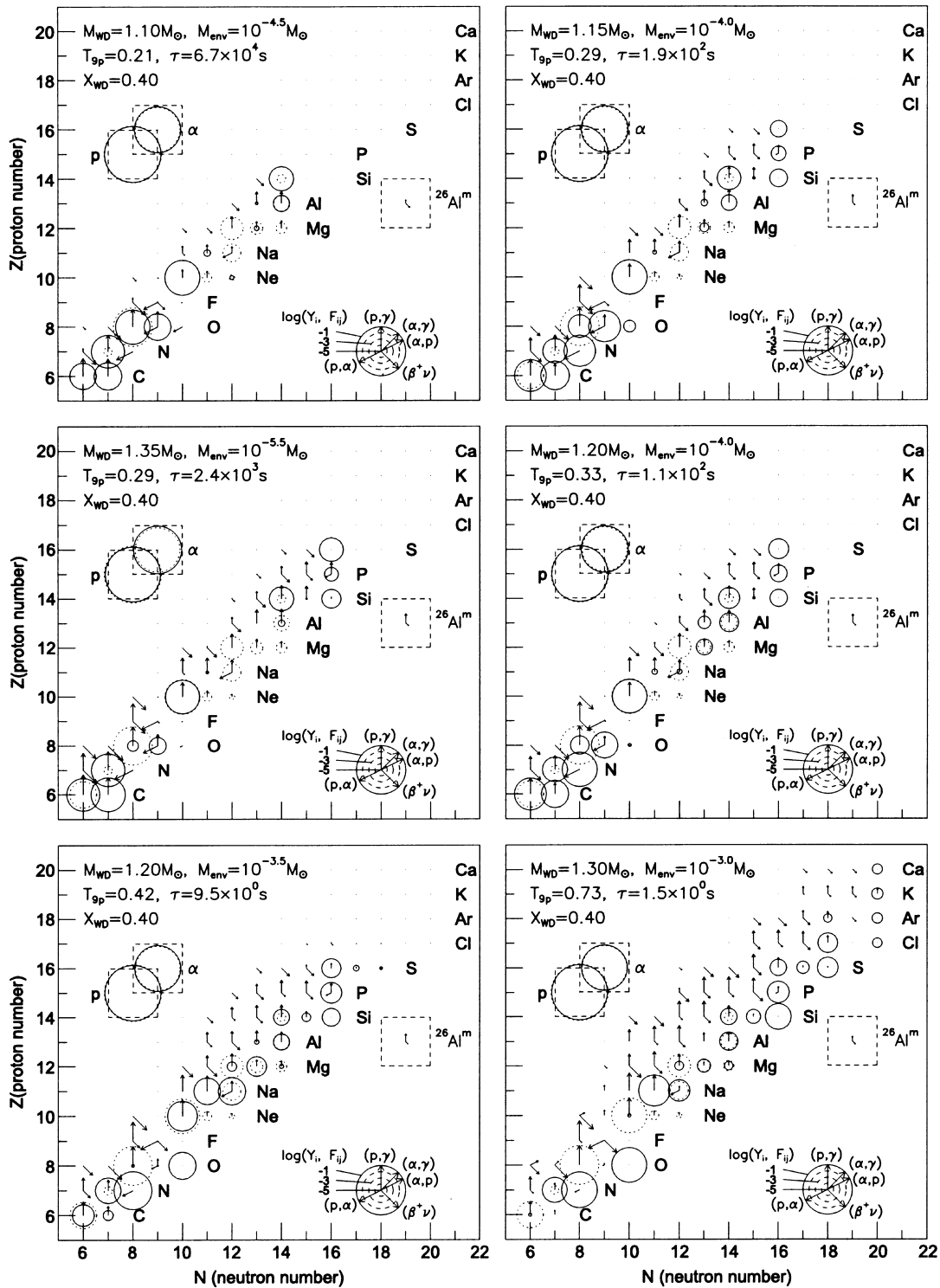FIG. 5.—Nucleosynthesis results for several $(M_{WD}/M_\odot, M_{env}/M_\odot)$ sequences in the N-Z plane. The size of each circle indicates the yield at the final stage, and the length of each arrow the net nuclear flow in the logarithmic scale. The initial compositions are shown by dotted circles.

(Gehrz et al. 1998, and references therein), the cooling timescale must be $\lesssim 1000$ s when the β^+-decay of ^{14}O ($\tau \simeq 102$ s) and ^{15}O ($\tau \simeq 176$ s) plays an important role.

4.1.1. Low-Temperature Sequences

For the model $(M_{WD}/M_\odot, M_{env}/M_\odot) = (1.10, 10^{-4.5})$, the initially present ^{24}Mg is entirely transferred to silicon, even though T_{peak} is as low as $\sim 2 \times 10^8$ K (Fig. 5). In contrast, the initial ^{20}Ne remains mostly unburned, though minor nuclear flows appear through the Ne–Na cycle. A part of

the initial ^{16}O is converted to ^{17}O, ^{12}C, ^{13}C, and ^{14}N. The HCNO cycle is active near the peak in temperature, turning to the CNO cycle as the temperature decreases. Thus, almost all ^{15}N is eventually converted to ^{14}N, ^{12}C, and ^{13}C. Note that, for the models with $T_{peak} \lesssim 2 \times 10^8$ K, v_{exp} is too small to overcome v_{esc}, as seen in Figure 6.

4.1.2. Moderate-Temperature Sequences

The nucleosynthesis results for $(M_{WD}/M_\odot, M_{env}/M_\odot) = (1.15, 10^{-4.0})$ and $(1.35, 10^{-5.5})$ (hereafter N1540B and
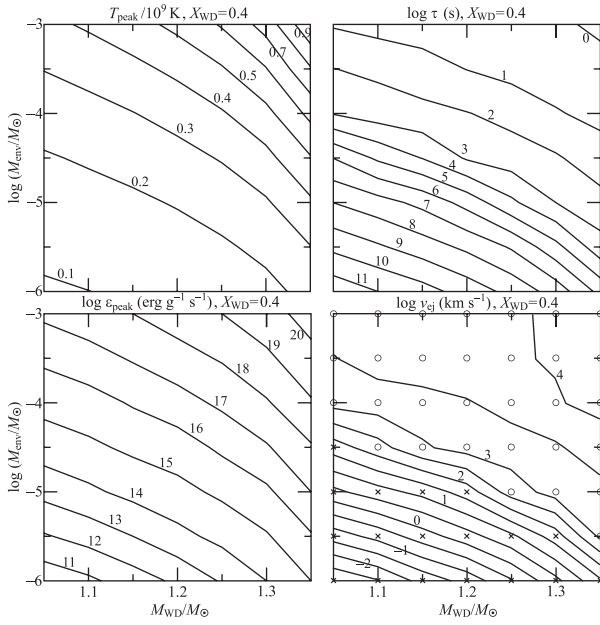
FIG. 6.—Contours of the peak temperatures at the base, the cooling timescales, the energy generation rates per unit mass, and the ejection velocities in the $M_{\rm WD}$-$M_{\rm env}$ space (case B).

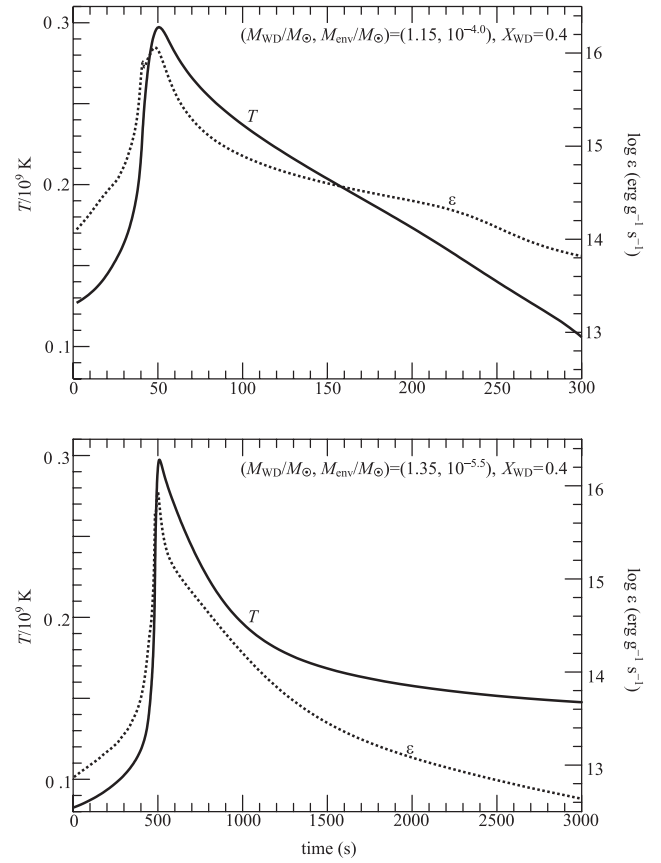FIG. 7.—Time variations of the temperature at the base and the nuclear energy generation rate per unit mass for $(M_{\rm WD}/M_\odot, M_{\rm env}/M_\odot) = (1.15, 10^{-4.0})$ and $(1.35, 10^{-5.5})$.

N3555B, respectively) differ significantly, regardless of their mostly same $T_{\rm peak}$ ($\simeq 2.9 \times 10^8$ K), as seen in Figure 5. This can be explained as follows. Figure 7 shows the time variations of T_b and ε for each model. The cooling timescale for N1540B ($\tau \simeq 190$ s) is more than 1 order shorter than for N3555B ($\tau \simeq 2400$ s). This is a consequence of the weaker gravitational potential for N1540B owing to its smaller $M_{\rm WD}$ and thus its larger $R_{\rm WD}$ (Fig. 3). In addition, the nuclear energy generation rate remains as high as $\sim 10^{14}$ ergs g^{-1} s^{-1} even after the envelope expands and the temperature decreases to $\sim 10^8$ K, owing to the β^+-decay of ^{14}O, ^{15}O, and other unstable nuclei. As a result, the expansion of the envelope is accelerated and then the temperature drops fairly quickly, even when its structure is returning to the static configuration. In contrast, for N3555B, almost all the short-lived β^+-unstable nuclei have decayed at the late phase. Hence, the temperature drops slowly with the decreasing nuclear energy generation rate. The patterns of the temperature decreases are, therefore, not similar between these models. The critical cooling timescale between the slow (N3555B) and fast (N1540B) expansion is $\tau \sim 1000$ s. The cooling timescale for N1540B is comparable to the β^+-decay lifetime of ^{15}O ($= 176$ s). As a result, ^{15}N survives the following (p, α) reactions and significantly enhances. For similar reasons, ^{18}O, ^{25}Mg, and ^{26}Al are prominent in N1540B, while they are absent in N3555B. Note that the somewhat higher $\varepsilon_{\rm peak}$ in N1540B is due to the higher density at the base (Fig. 2).

It is noteworthy that the net nuclear flows of ^{24}Mg(p, γ)^{25}Al have overcome the initial abundance of ^{24}Mg for both N1540B and N3555B (Fig. 5), owing to substantial nuclear flux from the Ne–Na region. It implies that the initial amount of ^{24}Mg does not significantly affect the production of isotopes $A \geq 24$ for the models $T_{\rm peak} \gtrsim 3 \times 10^8$ K. Note that N1540B also obtains significantly higher ejection velocity ($\simeq 2100$ km s^{-1}) than N3555B ($\simeq 1200$ km s^{-1}). As seen in Figure 6, for all the models with $T_{\rm peak} \gtrsim 3$

$\times 10^8$ K, $v_{\rm exp}$ exceeds $v_{\rm esc}$ and obtains $v_{\rm ej} \gtrsim 1000$ km s^{-1}, which is in good agreement with recent observations of ONeMg novae.

4.1.3. High-Temperature Sequences

For the models $(M_{\rm WD}/M_\odot, M_{\rm env}/M_\odot) = (1.20, 10^{-4.0})$ and $(1.20, 10^{-3.5})$ (hereafter N2040B and N2035B, respectively), substantial nuclear fluxes appear in the Ne–Na region because of their high $T_{\rm peak}$ ($\simeq 3.3 \times 10^8$ K and 4.2×10^8 K, respectively), as seen in Figure 5. In addition, various nuclear paths open in the Mg–S region. The abundance of ^{26}Al is highly enhanced in N2040B because of the substantial nuclear flux from the Ne–Na region via ^{23}Na(p, γ)^{24}Mg. On the other hand, ^{26}Al is less abundant in N2035B because of its higher peak temperature. Instead, ^{18}O, ^{22}Na, and ^{23}Na are highly enhanced in N2035B, since τ ($\simeq 9.5$ s) is comparable to the β^+-decay lifetimes of ^{18}Ne (2.4 s), ^{22}Mg (5.6 s), and ^{23}Mg (16 s). For the extremely high temperature ($T_{\rm peak} \simeq 7.3 \times 10^8$ K) model $(M_{\rm WD}/M_\odot, M_{\rm env}/M_\odot) = (1.30, 10^{-3.0})$, almost all the initial ^{20}Ne is burned out and the nuclear flow extends to calcium by the rp-process (Fig. 5). Leakage from the CNO cycle via the α-capture of ^{14}O and ^{15}O is apparent, though its contribution to the heavy element production is negligible.

4.2. Element and Isotope Production

In this section, we discuss the global trends of element production and isotope ratios in the $M_{\rm WD}$-$M_{\rm env}$ space, referring to the abundances of ONeMg nova ejecta estimated from recent observations. Table 4 shows the abundances for the recent six ONeMg novae, V693 CrA

TABLE 4
OBSERVED ONeMg NOVA ABUNDANCES

Nova	H	He	C	N	O	Ne	Mg	Al	Si	S	Z	Ref.
V693 CrA.......	2.8E−01	3.2E−01	5.1E−03	8.4E−02	1.2E−01	1.7E−01	7.6E−03	3.4E−03	2.6E−03		4.0E−01	1
V693 CrA.......	1.6E−01	1.8E−01	7.9E−03	1.4E−01	2.1E−01	2.7E−01	1.8E−02		6.9E−03		6.5E−01	2
V693 CrA.......	3.9E−01	2.0E−01	4.3E−03	8.0E−02	7.5E−02	2.3E−01	2.9E−03	1.9E−03	8.7E−03		4.1E−01	3
V1370 Aql	4.9E−02	8.8E−02	3.5E−02	1.4E−01	5.1E−02	5.2E−01	6.8E−03		1.8E−03	1.0E−01	8.6E−01	4
V1370 Aql	4.5E−02	1.0E−01	5.0E−02	1.9E−01	3.7E−02	5.6E−01	7.9E−03		4.6E−03		8.5E−01	2
QU Vul	3.0E−01	6.0E−01	1.0E−03	2.1E−02	1.6E−02	2.3E−02	1.7E−03		4.0E−02		1.0E−01	5
QU Vul	3.3E−01	2.7E−01	9.6E−03	7.4E−02	1.8E−01	8.7E−02	3.7E−03	9.9E−03	3.2E−02	1.2E−02	4.0E−01	2
V351 Pup	3.8E−01	2.4E−01	5.9E−03	7.4E−02	1.9E−01	1.1E−01		4.3E−03	1.9E−03		3.8E−01	6
V838 Her	6.0E−01	3.1E−01	1.2E−02	1.4E−02	2.5E−03	5.8E−02				2.8E−03	9.0E−02	3
V1974 Cyg......	1.8E−01	3.1E−01	5.4E−02	7.7E−02	2.7E−01	1.1E−01					5.1E−01	7

REFERENCES.—(1) Williams et al. 1985; (2) Andreä et al. 1994; (3) Vanlandingham et al. 1997; (4) Snijders et al. 1987; (5) Saizar et al. 1992; (6) Saizar et al. 1996; (7) Austin et al. 1996.

(Williams et al. 1985; Andreä et al. 1994; Vanlandingham et al. 1997), V1370 Aql (Snijders et al. 1987; Andreä et al. 1994), QU Vul (Saizar et al. 1992; Andreä et al. 1994), V351 Pup (Saizar et al. 1996), V838 Her (Vanlandingham et al. 1997), and V1974 Cyg (Austin et al. 1996). Note that the abundances of the elements not presented in the above references are assumed to be zero, thus involving errors of a few percent. The average metallicity for these ONeMg novae is $\simeq 0.43$ by mass. The mixing ratio $X_{\rm WD}$ is, therefore, assumed to be 0.4 (case B) throughout this section. However, V1370 Aql and V838 Her show significantly different metallicities from case B. The dependence on the initial composition is discussed in § 4.3.

When temperature is higher than $\sim 2 \times 10^8$ K, proton captures are fast enough to compete with the β^+-decay of various unstable isotopes. As a result, the nucleosynthesis results are significantly deviated from those in steady nuclear flows such as the CNO and Ne–Na cycles. Figures 8–14 show the final abundances and isotope ratios by mass in the $M_{\rm WD}$-$M_{\rm env}$ space. The abundances are shaded from white (0.1) to black (10^{-5}) in the logarithmic scale (except for beryllium and boron). In the rest of this paper, all abundances are given in mass fraction. As described below, we find that there exist two types of elements, namely, those correlated to $T_{\rm peak}$ (e.g., oxygen, neon, and sulfur) and to τ (e.g., carbon, sodium, and magnesium).

4.2.1. Beryllium and Boron

As seen in Figure 8, the abundance of ^{7}Be (in mass fraction) reaches $\sim 10^{-6}$ for $T_{\rm peak} \sim 2.5$–4×10^8 K (Fig. 6) by the α-capture of the initially present ^{3}He. For the same $T_{\rm peak}$, the lower $M_{\rm WD}$ models produce more ^{7}Be than higher ones. This is due to the higher densities for the formers as

FIG. 8.—Contours of the abundances of ^{7}Be and ^{11}B in the logarithmic scale (case B).

seen in Figure 2. When density is less than $\sim 10^3$ g cm^{-3} at temperature ~ 2–4×10^8 K, the proton capture of ^{7}Be is suppressed by its inverse reaction (Boffin et al. 1993). For $T_{\rm peak} \gtrsim 4 \times 10^8$ K, ^{7}Be decreases by its α-capture. As a result, the abundance of ^{11}B reaches $\sim 10^{-7}$. For $T_{\rm peak} \gtrsim 6 \times 10^8$ K, the abundance of ^{11}B decreases owing to the reaction ^{11}C(α, p).

4.2.2. Carbon and Nitrogen

In the steady flow of the CNO cycle ($\lesssim 2 \times 10^8$ K), the most abundant isotope is ^{14}N and the isotope ratios are determined by the nuclear reaction rates as

$$^{12}{\rm C}/^{13}{\rm C} = \lambda[^{13}{\rm C}(p, \gamma)]/\lambda[^{12}{\rm C}(p, \gamma)] \sim 2\text{–}4 \ ,$$

$$^{14}{\rm N}/^{15}{\rm N} = \lambda[^{15}{\rm N}(p, \alpha)]/\lambda[^{14}{\rm N}(p, \gamma)] \sim 5000\text{–}50{,}000 \ .$$

When temperature exceeds $\sim 2 \times 10^8$ K, the CNO cycle is replaced with the HCNO cycle via ^{13}N$(p, \gamma)^{14}$O$(\beta^+, \nu)^{14}$N. The abundance patterns of the carbon and nitrogen (Fig. 9) mainly depend on τ (Fig. 6) as follows. (1) For $\tau \gg 1000$ s, the carbon and nitrogen isotopes show the typical feature of the steady CNO cycle, i.e., C/N $\ll 1$, ^{12}C/^{13}C ~ 3, and ^{14}N/^{15}N $\sim 30{,}000$. (2) For $\tau \sim 1000$ s, however, these isotope ratios approach ~ 1, because of the β^+-decay lifetimes of ^{13}N ($\simeq 862$ s) and ^{15}O ($\simeq 176$ s), which are comparable to the cooling timescale. The thermonuclear runaway ceases before most ^{13}N (and some ^{15}O) decays, and thus the ratio C/N also reaches ~ 1. (3) For $\tau \ll 1000$ s, the thermonuclear runaway ceases during the active HCNO cycle where ^{14}O and ^{15}O are abundant, resulting in C/N $\ll 1$. The ratio ^{12}C/^{13}C is unchanged (~ 3), while ^{14}N/^{15}N is significantly reduced, to ~ 0.1.

The abundance of nitrogen is ~ 0.1 in the whole area of the $M_{\rm WD}$-$M_{\rm env}$ space, regardless of the ratio ^{14}N/^{15}N ranging over 5 orders of magnitude. In contrast, the abundance of carbon ranges widely (~ 0.001–0.1), reaching its maximum at $\tau \sim 1000$ s, while the ratio ^{12}C/^{13}C is not significantly changed in the $M_{\rm WD}$-$M_{\rm env}$ space. The above results explain the abundance feature of the recent ONeMg novae (Table 4), in which the abundance of carbon spreads widely (~ 0.001–0.01) while that of nitrogen is ~ 0.1. Note that the abundance of nitrogen for QU Vul (Saizar et al. 1992) and V838 Her (Vanlandingham et al. 1996) is as low as ~ 0.02, owing to the significantly lower metallicities (~ 0.1). For V838 Her and V1974 Cyg, the ratio of C/N is ~ 1, which is obtained by the models with $\tau \sim 1000$ s.

It should be noted that our models may significantly underproduce ^{15}N, which causes the too-large ratio C/N as discussed in § 3. This may be, however, the case only in the

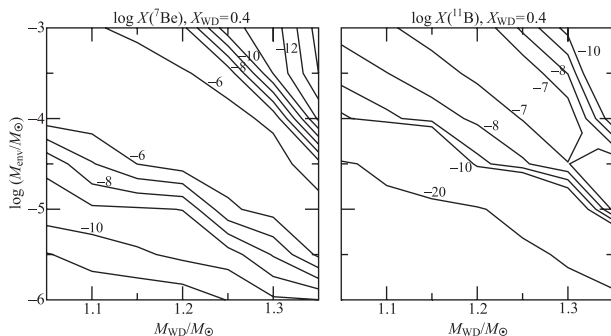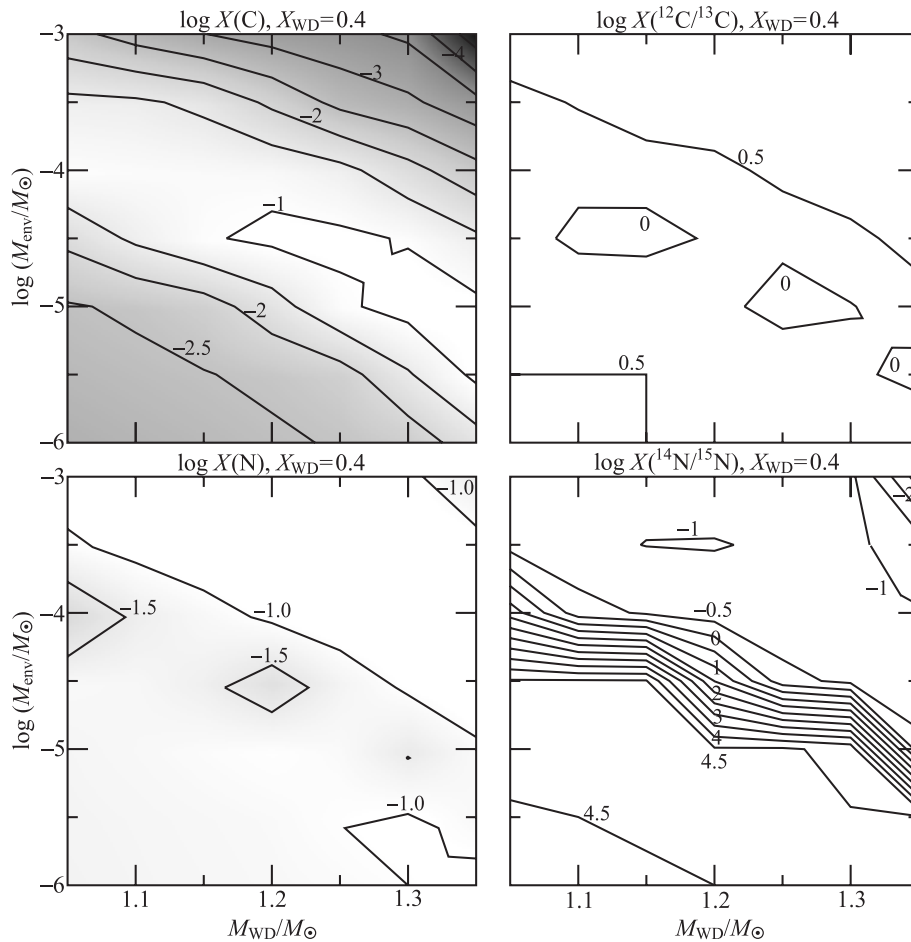FIG. 9.—Same as Fig. 8, but for carbon and nitrogen and their isotope ratios

models with $\tau \gg 1000$ s. For the models with $\tau \lesssim 1000$ s, the abundance of ^{15}N is not significantly reduced as described above, and thus the results may not be changed substantially.

4.2.3. *Oxygen and Fluorine*

The abundance of oxygen is mainly correlated to T_{peak} but is also dependent on τ (Fig. 10), owing to the presence of three isotopes. The ratio ^{16}O/^{17}O has a clear correlation with T_{peak}. It reaches the minimum (~ 0.3) at $T_{peak} \sim 3 \times 10^8$ K and is nearly constant (~ 3 for $T_{peak} \lesssim 2 \times 10^8$ K and ~ 10 for $T_{peak} \gtrsim 4 \times 10^8$ K) because of the different nuclear reaction cycles (Fig. 5). In contrast, the ratio ^{16}O/^{18}O shows a clear correlation with the cooling timescale (Fig. 10), being significantly small for $\tau \lesssim 100$ s. As a result, the abundance of oxygen reaches ~ 0.03–0.1 for (1) $T_{peak} \lesssim 3 \times 10^8$ K (^{16}O and ^{17}O are abundant) or for (2) $\tau \lesssim 100$ s (^{18}O is abundant). Note that oxygen is always abundant in the models with $M_{WD} \lesssim 1.15 M_\odot$, where one of these conditions is satisfied.

Fluorine (^{19}F) is not significantly enhanced in the all models (Fig. 10). The reason is that the reaction ^{18}F(p, γ)^{19}Ne, which is followed by the β^+-decay to ^{19}F, is much slower than ^{18}F(p, α)^{15}O. The abundance of ^{19}F is $\sim 10^{-4}$ at most for $\tau \sim 10$ s, which is comparable to the β^+-decay lifetime of ^{19}Ne ($\simeq 25$ s).

The oxygen-rich ONeMg novae (~ 0.1–0.3 by mass) V693 CrA, QU Vul, V351 Pup, and V1974 Cyg (Table 4) can be explained by the following models: (1) $M_{WD} \lesssim 1.15$

$M_\odot$, (2) $T_{peak} \lesssim 2 \times 10^8$ K, and (3) $\tau \lesssim 10$ s. On the other hand, V838 Her is fairly oxygen poor ($\simeq 3.3 \times 10^{-3}$), which could be explained by a rather massive model ($M_{WD} \sim 1.3 M_\odot$). It should be noted, however, that its estimated metallicity is $\simeq 0.09$ (Table 4), significantly less than assumed in this section (see § 4.3).

The ratio C/O can be $\gtrsim 1$ for $\tau \sim 1000$ s where the abundance of carbon is ~ 0.1 and that of oxygen is $\lesssim 0.1$. It implies that the carbon-rich ONeMg novae, i.e., V1370 Aql and V838 Her, may be explained by the models with $\tau \sim 1000$ s. Note that carbon tends to be overproduced in the models with $\tau \gg 1000$ s (§ 4.2.2). This may not, however, change the above result with $\tau \sim 1000$ s.

4.2.4. *Neon and Sodium*

Neon is the second most abundant metal in the initial composition (Table 3). The abundance of neon is not significantly reduced for $T_{peak} \lesssim 4 \times 10^8$ K because of its rather slow proton capture (Fig. 11). Nevertheless, the substantial nuclear flow appears in the Ne–Na cycle even for $T_{peak} \sim 2$–3×10^8 K (Fig. 5) owing to the abundant neon initially present. The ratio ^{20}Ne/^{21}Ne is clearly correlated with the cooling timescale, being small for the shorter τ, where the β^+-decay lifetime of ^{21}Na ($\simeq 32$ s) is not negligible. On the other hand, the ratio ^{20}Ne/^{22}Ne is clearly correlated to the peak temperature, increasing with a rise in T_{peak}. This is due to the faster proton capture on ^{22}Ne than on ^{20}Ne.

The abundance of sodium is $\lesssim 10^{-3}$ for $\tau \gtrsim 100$ s, because of the steady Ne–Na cycle, where ^{20}Ne is most
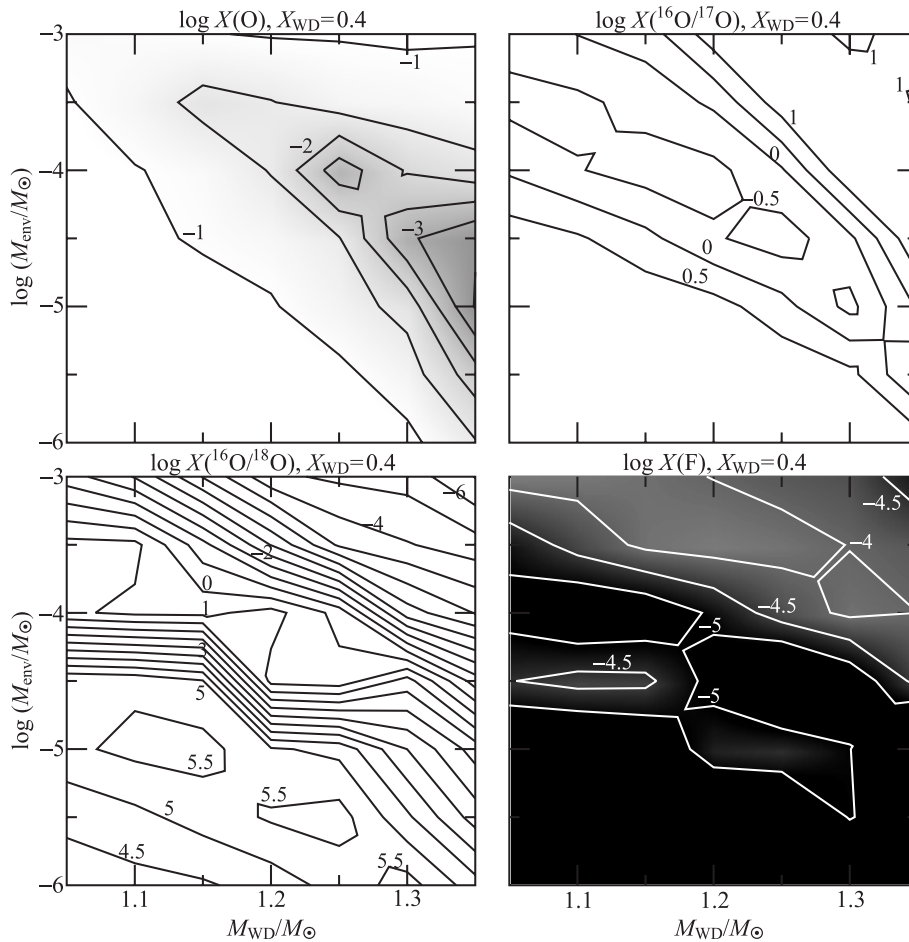
FIG. 10.—Same as Fig. 8, but for oxygen, its isotope ratios, and fluorine

abundant (Fig. 11). The isotope ratio is also determined by their reaction rates as

$$^{22}\mathrm{Na}/^{23}\mathrm{Na} = \lambda[^{23}\mathrm{Na}(p, \alpha)]/\lambda[^{22}\mathrm{Na}(p, \gamma)] \sim 10 \;,$$

in the temperature range ~ 2–4×10^8 K. On the other hand, sodium is abundant (~ 0.01–0.1 by mass) for $\tau \lesssim 100$ s, where the β^+-decay lifetimes of $^{22}\mathrm{Mg}$ ($\simeq 6$ s) and $^{23}\mathrm{Mg}$ ($\simeq 16$ s) are not negligible. Thus, a part of sodium, which is the decayed product of the magnesium isotopes, survives the subsequent proton capture. The ratio $^{22}\mathrm{Na}/^{23}\mathrm{Na}$ reaches ~ 1, owing to the abundant $^{22}\mathrm{Mg}$ and $^{23}\mathrm{Mg}$ in the Ne–Na region during outbursts. The abundance of $^{22}\mathrm{Na}$ shows a similar trend to that of sodium, clearly correlated to the cooling timescale. This abundance can be changed by the large uncertainty of the $^{22}\mathrm{Na}(p, \gamma)^{23}\mathrm{Mg}$ rate (Kubono et al. 1994, 1997; Schmidt et al. 1995; Coc et al. 1995). However, it may not be significantly affected for $\tau \lesssim 100$ s, since the explosive burning ceases while $^{22}\mathrm{Mg}$ is abundant.

The enrichment in neon is characteristic of all the observed ONeMg novae. On the other hand, no positive detection of sodium has been reported for recent ONeMg novae (Gehrz et al. 1994) because of a lack of useful lines and, probably, little enrichment in sodium in the nova ejecta. An alternative way to check the nucleosynthesis in the Ne–Na region is to compare with the result of the γ-ray line survey of the $^{22}\mathrm{Na}$ decay from a nearby ONeMg nova by the *Compton Gamma-Ray Observatory* (*CGRO*) or *International Gamma-Ray Astrophysical Laboratory* (*INTEGRAL*) in the near future.

4.2.5. *Magnesium and Aluminum*

Magnesium is one of the abundant elements initially present, but it is rather fragile against proton capture. As a result, it is mostly transferred to aluminum and silicon via the opened Mg–Al cycle (Timmermann et al. 1988; Champagne et al. 1988). As seen in Figure 12, the abundance of magnesium reaches its minimum at $\tau \sim 1000$ s, in contrast to carbon (Fig. 9). For $\tau \lesssim 1000$ s, it reaches $\sim 10^{-2}$ because of the substantial leakage from the Ne–Na cycle and the nonnegligible β^+-decay lifetime of $^{25}\mathrm{Al}$ ($\simeq 10$ s). Note that the most abundant isotope is always $^{25}\mathrm{Mg}$ because it has the slowest proton capture. The isotope ratios $^{24}\mathrm{Mg}/^{25}\mathrm{Mg}$ and $^{24}\mathrm{Mg}/^{26}\mathrm{Mg}$ are clearly correlated with the cooling timescale. They are, however, not monotonic with τ but complicated because of the inflow from the Ne–Na cycle and the leakage from the Mg–Al region and the various nuclear paths at high temperature (Fig. 5).

The abundance of aluminum shows a similar trend to that of magnesium, correlated to the cooling timescale (Fig. 12). The ratio $^{26}\mathrm{Al}/^{27}\mathrm{Al}$ is not significantly changed, being close to

$$^{26}\mathrm{Al}/^{27}\mathrm{Al} = \lambda[^{27}\mathrm{Al}(p, \gamma)]/\lambda[^{26}\mathrm{Al}(p, \gamma)] \sim 0.1\text{–}0.5$$

in the temperature range ~ 1–4×10^8 K. However, the ratio decreases with a reduction in the cooling timescale because of the nonnegligible β^+-decay lifetime of $^{27}\mathrm{Si}$ ($\simeq 6$ s) that is the parent isotope of $^{27}\mathrm{Al}$. Note that, for rather high temperature models ($T_{\mathrm{peak}} \gtrsim 4 \times 10^8$ K), the proton

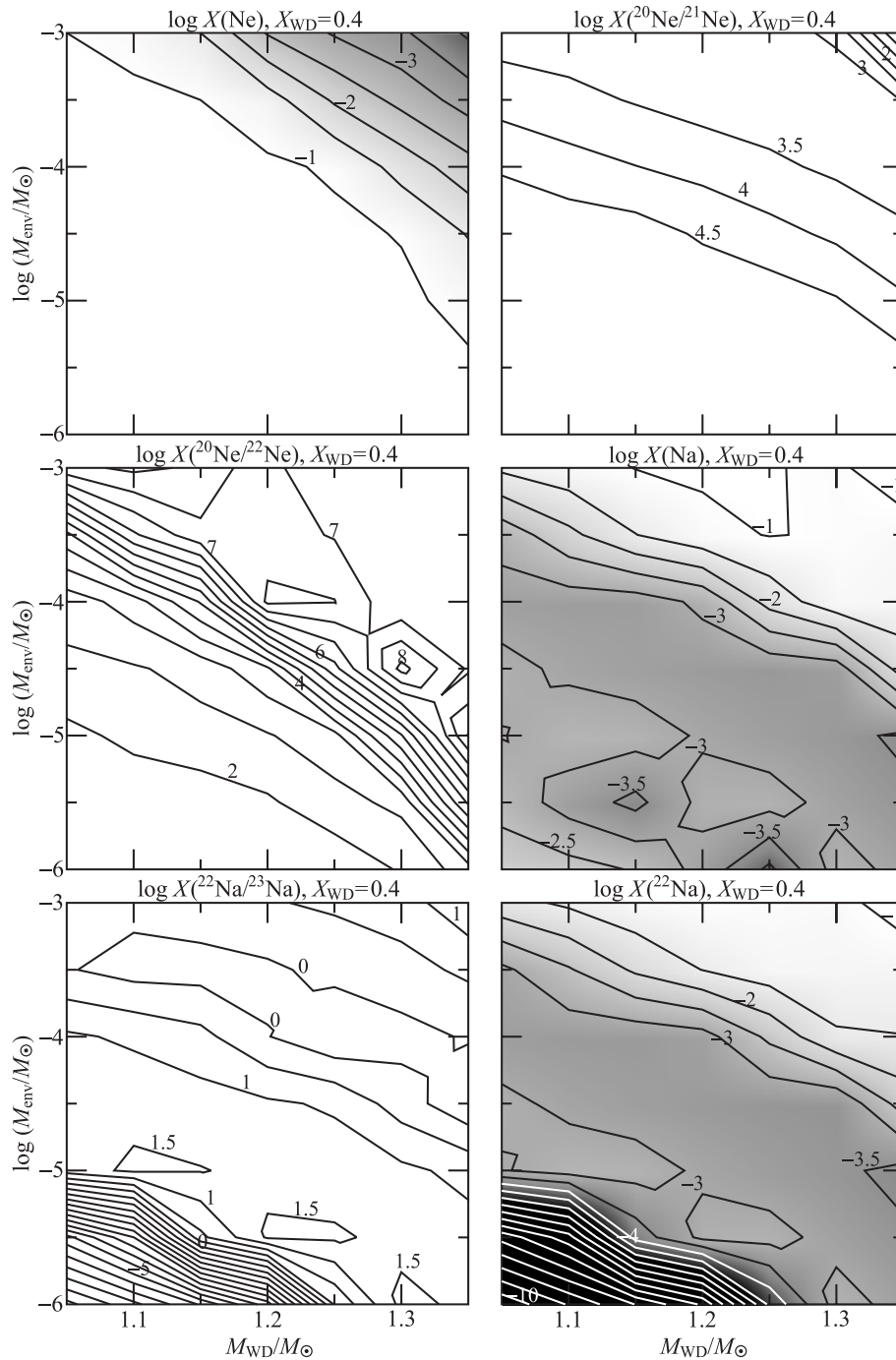FIG. 11.—Same as Fig. 8, but for neon, sodium, their isotope ratios, and ^{22}Na

capture on ^{25}Al is faster than its β^+-decay. The subsequent isotope ^{26}Si decays to ^{26}Mg in ~ 12 s through the isomeric state of ^{26}Al, bypassing its ground state. The double peaks in ^{26}Al ($\sim 3 \times 10^{-3}$ by mass) can be seen in Figure 12. The one at lower peak temperatures ($\sim 1.8 \times 10^8$ K) is consistent with those of PSTWS95, STWS98, and JH98, in which the abundance of ^{26}Al decreases with increasing white dwarf mass. The other peak at higher peak temperatures ($\gtrsim 3 \times 10^8$ K) is the consequence of the substantial nuclear flux from the Ne–Na region. The latter peak, which has not been presented in the previous works, is of importance on whether ONeMg novae can be the significant contributors of the Galactic ^{26}Al. Note that the abundance of ^{26}Al in the latter case does not substantially depend on the initial abundance of ^{24}Mg (§ 4.1). There are large uncertainties in the reaction rates of ^{25}Al$(p, \gamma)^{26}$Si (Wiescher et al. 1986; Coc et al. 1995; Iliadis et al. 1996), ^{26}Si$(p, \gamma)^{27}$P (Herndl et al. 1995), ^{25}Mg$(p, \gamma)^{26}$Al (Coc et al. 1995; Iliadis et al. 1996), and ^{26}Al$(p, \gamma)^{27}$Si (Coc et al. 1995; Champagne, Brown, & Sherr 1993; Coc et al. 1995). Our trial calculations for a few models suggest that these uncertainties change the abundance of ^{26}Al by a factor of ~ 2–3.

The clear dependence of magnesium on the cooling timescale is useful to constrain ($M_{\rm WD}$, $M_{\rm env}$) for observed ONeMg novae. The estimated abundance of magnesium is $\sim 4 \times 10^{-3}$ to 2×10^{-2} for V693 CrA, V1370 Aql, and QU
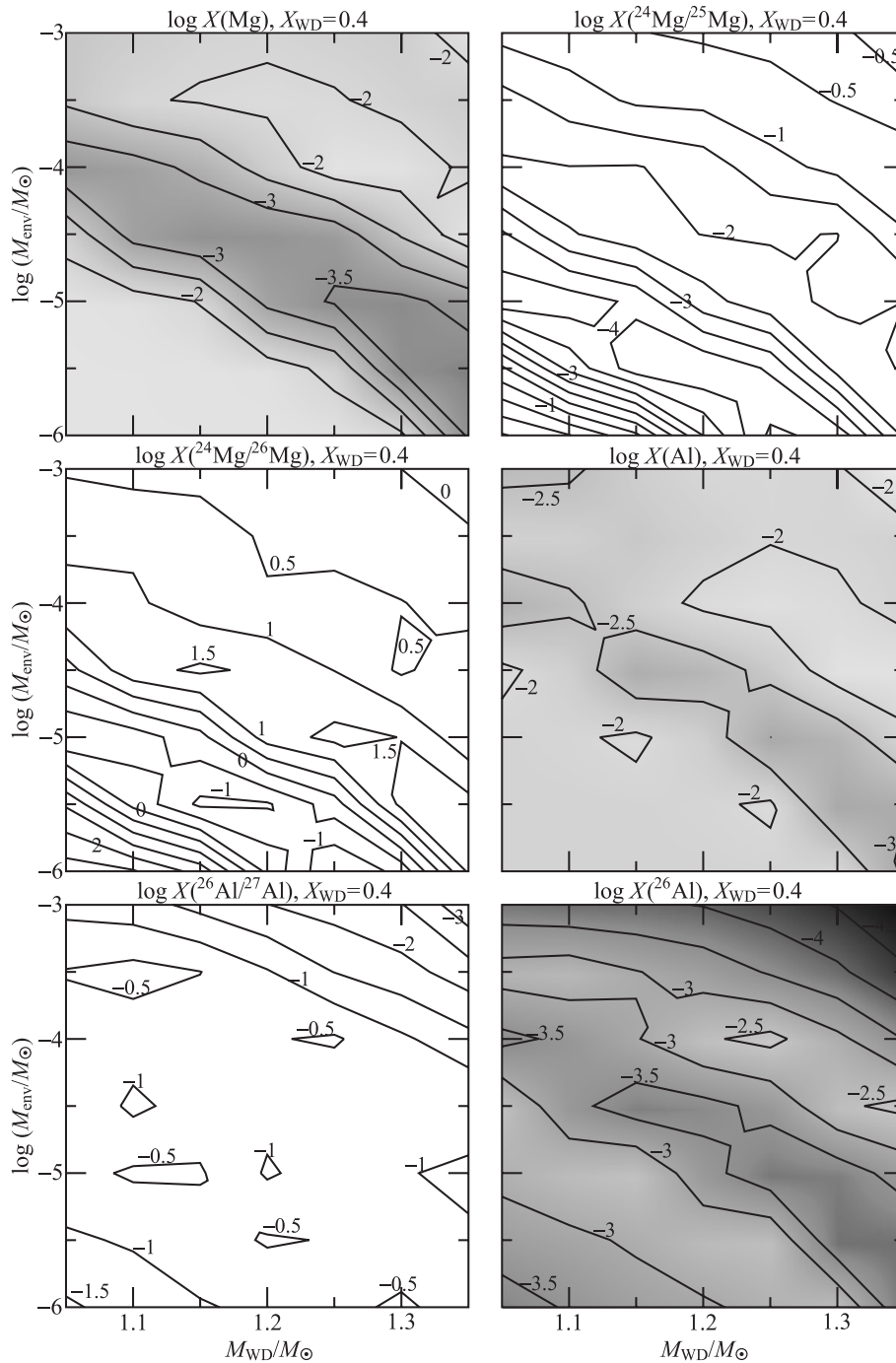
FIG. 12.—Same as Fig. 8, but for magnesium, aluminum, their isotope ratios, and ^{26}Al

Vul (Table 4), corresponding to $\tau \lesssim 100$ s or $\tau \gtrsim 10^6$ s (see Figs. 6 and 12). The abundance of aluminum does not significantly vary in the M_{WD}-M_{env} space, being not useful to constrain (M_{WD}, M_{env}). Nevertheless, the abundance estimates of aluminum are $\sim 3 \times 10^{-3}$ to 10^{-2} for V693 CrA, QU Vul, and V351 Pup (Table 4), which is in good agreement with our results.

4.2.6. Silicon and Phosphorus

The abundance of silicon reaches $\sim 3 \times 10^{-2}$ for $T_{peak} \gtrsim 2 \times 10^8$ K (Fig. 13) via the substantial nuclear flux from the Mg–Al region. The abundance is only weakly correlated to the cooling timescale. On the other hand, the ratios ^{28}Si/^{29}Si and ^{28}Si/^{30}Si are clearly correlated with o the cooling

timescale because of various competitions between proton capture and β^+-decay (Fig. 5).

The abundance of phosphorus (^{31}P) reaches $\sim 10^{-3}$ to 10^{-2} for $T_{peak} \gtrsim 3 \times 10^8$ K because of the faster proton capture on ^{30}P than its β^+-decay (Fig. 13). Since the Si–P cycle is not closed, as seen in Figure 5, phosphorus is not significantly destroyed.

The abundance of silicon in the ejecta of V693 CrA, V1370 Aql, and V351 Pup is as small as ~ 2–7×10^{-3}, corresponding to $T_{peak} \lesssim 2 \times 10^8$ K. In contrast, that in QU Vul (~ 3–4×10^{-2}) is in agreement with the models $T_{peak} \gtrsim 2 \times 10^8$ K. The discovery of phosphorus has been reported in the ejected shell of V1974 Cyg by near-infrared spectroscopy (Wagner & DePoy 1996). It suggests that
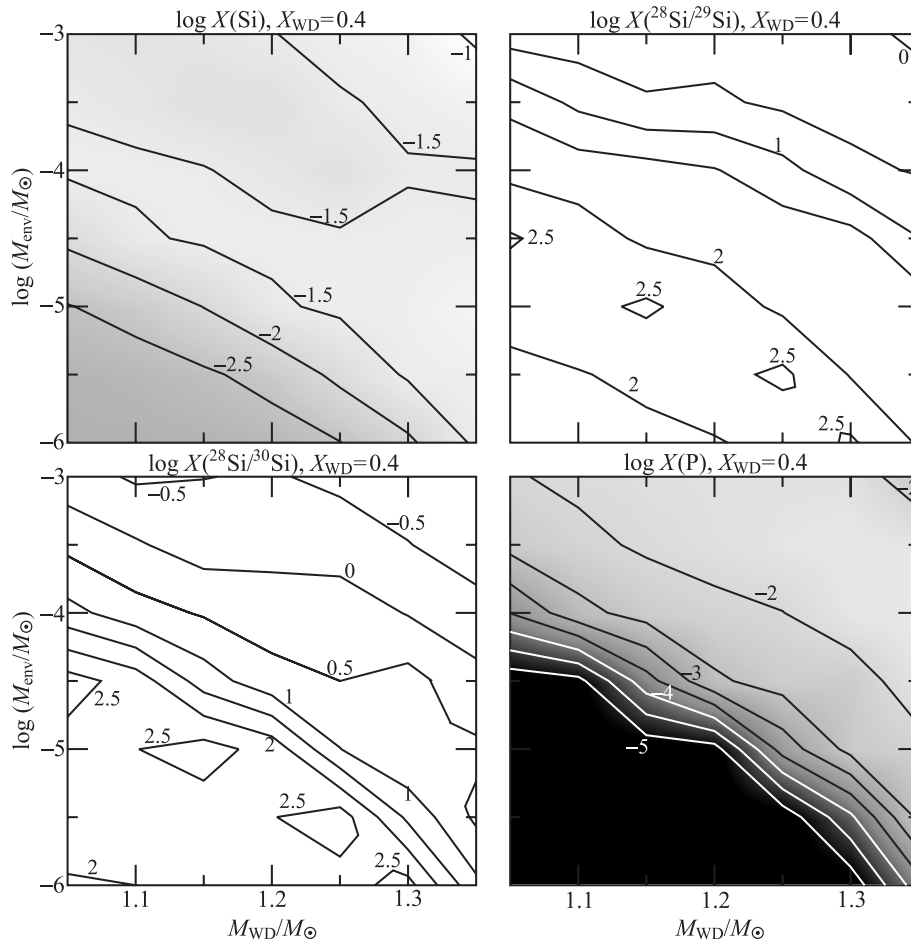
Fig. 13.—Same as Fig. 8, but for silicon, its isotope ratios, and phosphorus

V1974 Cyg can be explained by a model with a rather high peak temperature, although an accurate abundance of phosphorus is required to constrain (M_{WD}, M_{env}). It is also interesting to note that significantly enhanced phosphorus has been detected on the white dwarf in a dwarf nova system (Sion et al. 1997) and in the broad-line system of a QSO (Shields 1996), which might originate from ONeMg novae.

4.2.7. Sulfur and Other Heavy Elements

The abundance of sulfur reaches $\sim 10^{-2}$ for $T_{peak} \gtrsim 3 \times 10^8$ K through leakage from the Si–P region (Fig. 14). The abundance does not exceed 10^{-2} in the models $M_{WD} \lesssim 1.15$ $M_\odot$ because of the shorter cooling timescale (Fig. 6). This condition is, however, highly dependent on the initial composition, as will be discussed in § 4.3. For $T_{peak} \gtrsim 3 \times 10^8$ K, the ratios ^{32}S/^{33}S and ^{32}S/^{34}S decrease with a rise in peak temperature because of the increasing nuclear paths (Fig. 5). For $T_{peak} \lesssim 3 \times 10^8$ K, these ratios approach those determined by their reaction rates.

At least one-half of the observed ONeMg novae, V1370 Aql, QU Vul, and V838 Her, are abundant in sulfur in their ejecta (Table 4). In addition, the sulfur enrichment has been confirmed in the V1974 Cyg ejecta from near infrared spectroscopy (Woodward et al. 1992, 1995; Wagner & DePoy 1996). These novae can be explained by the models with such high peak temperatures as $T_{peak} \gtrsim 3 \times 10^8$ K. The estimated abundance of sulfur for V1370 Aql is much higher

than by any models in the M_{WD}-M_{env} space (Fig. 14). It should be noted, however, the estimated metallicity for V1370 Aql is twice as much as assumed in this section (see § 4.3).

Heavier elements, from chlorine to calcium, are not substantially enhanced for $T_{peak} \lesssim 4 \times 10^8$ K (Fig. 14). In addition, their enhancement is never seen in the models with $M_{WD} \lesssim 1.15$ $M_\odot$ because of the shorter cooling timescale. Nevertheless, the enrichment in chlorine has been reported for the ejecta of V1974 Cyg by near-infrared spectroscopy (Wagner & DePoy 1996). The accurate abundance of chlorine would severely constrain (M_{WD}, M_{env}) for V1974 Cyg.

4.3. Dependence on the Initial Composition

So far we have discussed the nucleosynthesis results for only one set of the initial composition $X_{WD} = 0.4$ (case B). However, the metallicities of the ejecta for V1370 Aql and QU Vul by Saizar et al. (1992) and for V838 Her deviate significantly from 0.4 (Table 4). In addition, the different authors present different metallicity estimates for the same nova events. In particular, the discrepancy is serious for QU Vul between Saizar et al. (1992) ($\simeq 0.10$) and Andreä et al. (1994) ($\simeq 0.40$). It is therefore difficult to judge whether the dispersion of the metallicities is real or due to observational errors. In the following, we discuss how the initial composition influences the nucleosynthesis results, comparing the low- ($X_{WD} = 0.1$; case A) and high- ($X_{WD} = 0.8$; case C) metallicity cases.
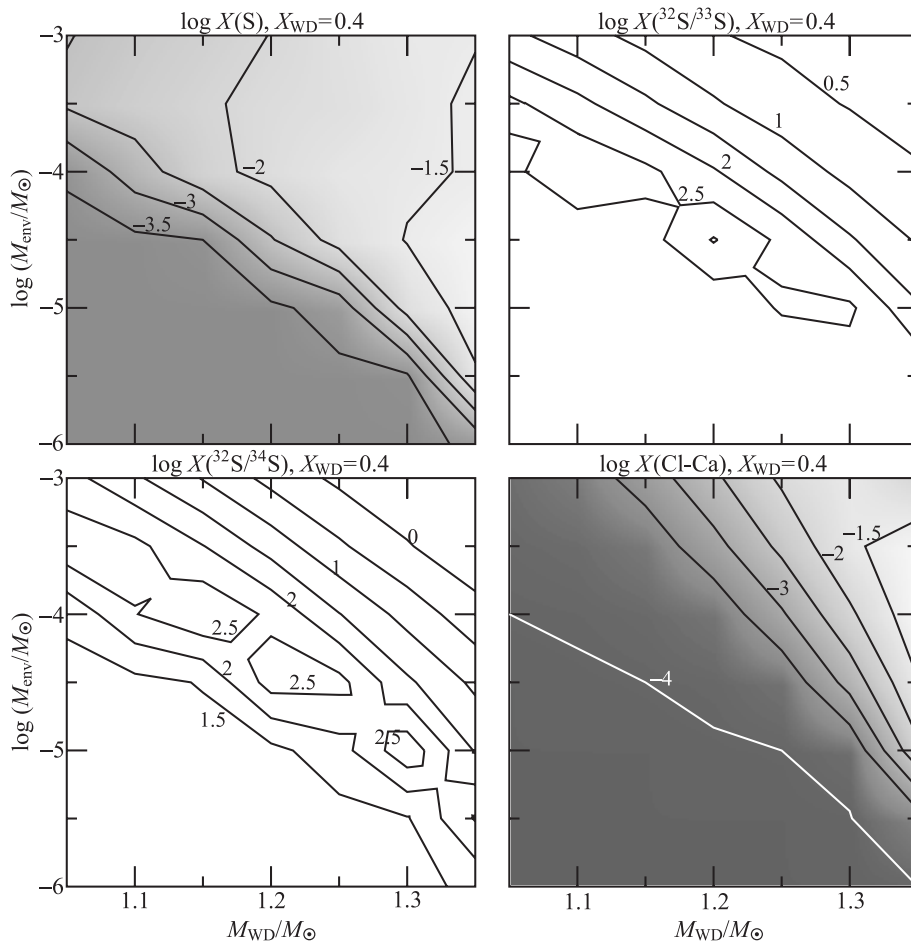
FIG. 14.—Same as Fig. 8, but for sulfur and its isotope ratios, and the sum of chlorine, argon, potassium, and calcium

As discussed in § 2.1, the density and temperature structures of an envelope are determined uniquely by a set of $(M_{\rm WD}, M_{\rm env})$ in our model, being independent of its time evolution (but slightly dependent on the time variation in mean molecular weight). As a result, case C is at most 20% higher than case A in peak temperature for each $(M_{\rm WD}, M_{\rm env})$, as seen in Figure 15. The higher temperature in case C is due to the larger mean molecular weight. In contrast, a variation in initial composition is crucial for the cooling timescale (Fig. 15). For $T_{\rm peak} \gtrsim 2 \times 10^8$ K, case C is more than 10 times shorter than case A in τ. This is a consequence of the higher nuclear energy in case C (Fig. 16) because of the abundant nuclear fuel. The ejection velocity is also affected by the initial composition. As seen in Figure 16, case C reaches significantly higher $v_{\rm ej}$ than case A in each model.

A prominent distinction between case A (N0540A) and case C (N0540C) can be seen in Figure 17, which shows the nuclear flows and the final yields in the model $(M_{\rm WD}/M_\odot, M_{\rm env}/M_\odot) = (1.05, 10^{-4.0})$. In N0540A, the nuclear flow extends to sulfur because of the longer cooling timescale ($\simeq 23,000$ s), while that in N0540C ($\tau \simeq 1800$ s) extends to silicon. Model N0540A consumes most of oxygen initially present, in contrast to N0540C.

Figures 18, 19, and 20 show the abundances of important elements and γ-ray emitters in the $M_{\rm WD}$-$M_{\rm env}$ space for case A and case C. These results are explained as follows:

1. The abundance of carbon is still clearly correlated to τ as in case B (§ 4.2.2), reaching its maximum at $\tau \sim 1000$ s for both cases (Fig. 18). The abundance is roughly proportional to $X_{\rm WD}$ among the models with the same cooling timescale.

2. Magnesium is another element clearly correlated to τ as in case B (§ 4.2.5). In case A, the abundance is significantly smaller than in case C, not enhanced even for $\tau \lesssim 1000$ s. This is a consequence of the longer τ in case A, where the nuclear flow extends to heavier elements than magnesium (Fig. 17).

3. Silicon is also an element showing a correlation to τ in case B, not significantly changed for $T_{\rm peak} \gtrsim 2 \times 10^8$ K (§ 4.2.6). This feature holds for case C. However, the abundance in case A has a correlation to $T_{\rm peak}$ rather than τ, reaching its maximum at $T_{\rm peak} \sim 2.5 \times 10^8$ K (Fig. 19). The depletion of silicon in case A for high $T_{\rm peak}$ is due to the long cooling timescale.

4. The trend of oxygen abundance significantly differs between case A and case C (Fig. 18). The abundance in case B is correlated to both $T_{\rm peak}$ and τ, being more abundant in the lower $M_{\rm WD}$ models (§ 4.2.3). In case C, however, the abundance is not significantly changed in the $(M_{\rm WD}, M_{\rm env})$ space, being ~ 0.3. On the other hand, that in case A is clearly correlated to the peak temperature, significantly depleted for $T_{\rm peak} \gtrsim 2.5 \times 10^8$ K (Fig. 18).

5. The abundance of sulfur shows a correlation to $T_{\rm peak}$ in all cases. In case C, however, the abundance is $\lesssim 10^{-3}$ for
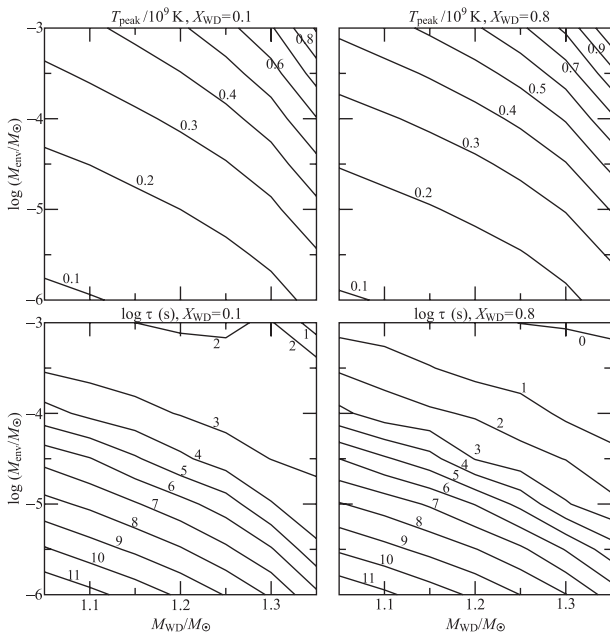
FIG. 15.—Contours of the peak temperatures at the base and the cooling timescales in the M_{WD}-M_{env} space for case A and C
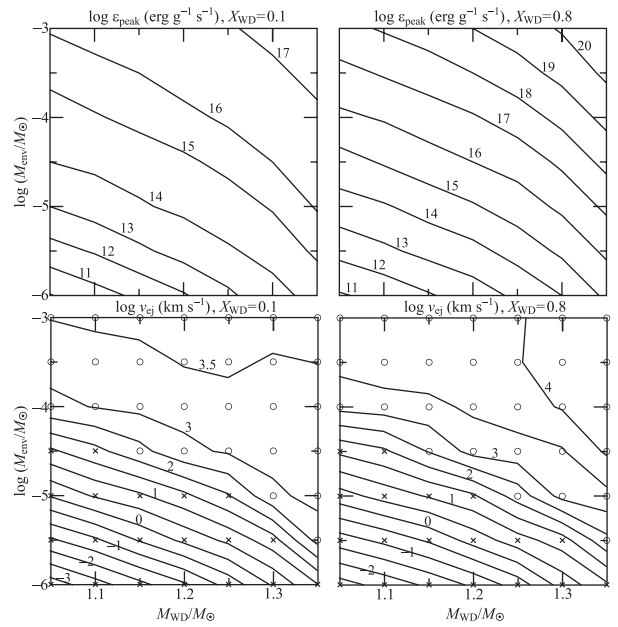

FIG. 16.—Same as Fig. 15, but for the energy generation rates per unit mass and the ejection velocities.

the models $M_{WD} \lesssim 1.15$ $M_\odot$ because of the shorter τ. On the other hand, that in case A reaches $\sim 3 \times 10^{-2}$ at $\gtrsim 3 \times 10^8$ K, since τ is longer and thus the nuclear flow extends to heavier elements.

6. The radioactive species ^{7}Be, ^{22}Na, and ^{26}Al are not significantly enhanced in case A because of its longer cooling timescale (Fig. 20). On the other hand, these abundances in case C show trends similar to those in case B in the M_{WD}-M_{env} space (Fig. 8).

The estimated metallicity for the ejecta of V1370 Aql is extremely high, $Z \sim 0.85$ (Table 4), which is close to the value in case C. However, the abundance of oxygen is significantly small (~ 4–5×10^{-2}), being inconsistent with our

results ($\gtrsim 0.1$). In addition, sulfur in the ejecta is extremely abundant (~ 0.1 by mass), which is also in disagreement with our results ($\lesssim 10^{-2}$). These features, i.e., the low abundances of oxygen and high abundances of sulfur, could be explained by lower X_{WD} models rather than higher ones (Figs. 10, 14, 18, and 19). Thus, the extremely high metallicity in this nova ejecta may not be real but due to difficulties in the observational estimates.

For the QU Vul ejecta, Saizar et al. (1992) gave a much lower metallicity estimate ($Z \simeq 0.10$) corresponding to case A than Andreä et al. (1994). The low abundance estimates of carbon, oxygen, and magnesium by Saizar et al. (1992) are in good agreement with our results for $T_{peak} \lesssim 2 \times 10^8$ K (Figs. 15, 18, and 19). However, the abundance of silicon ($\sim 4 \times 10^{-2}$ by mass) suggests that the nova has reached
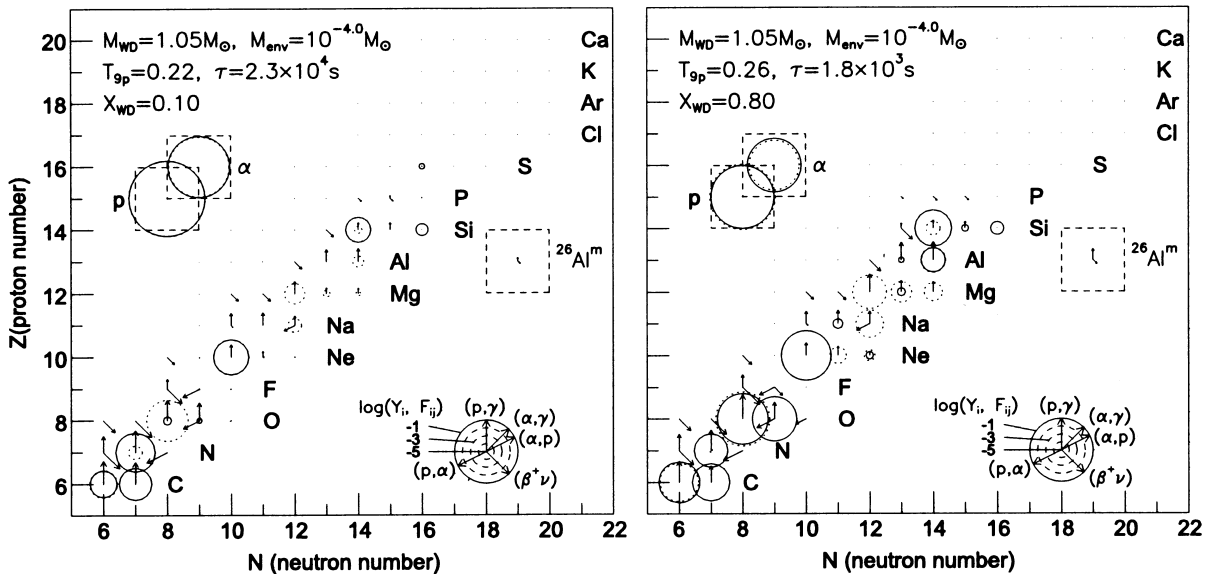

FIG. 17.—Nucleosynthesis results for $(M_{WD}/M_\odot, M_{env}/M_\odot) = (1.05, 10^{-4.0})$ in the N-Z plane for case A and C
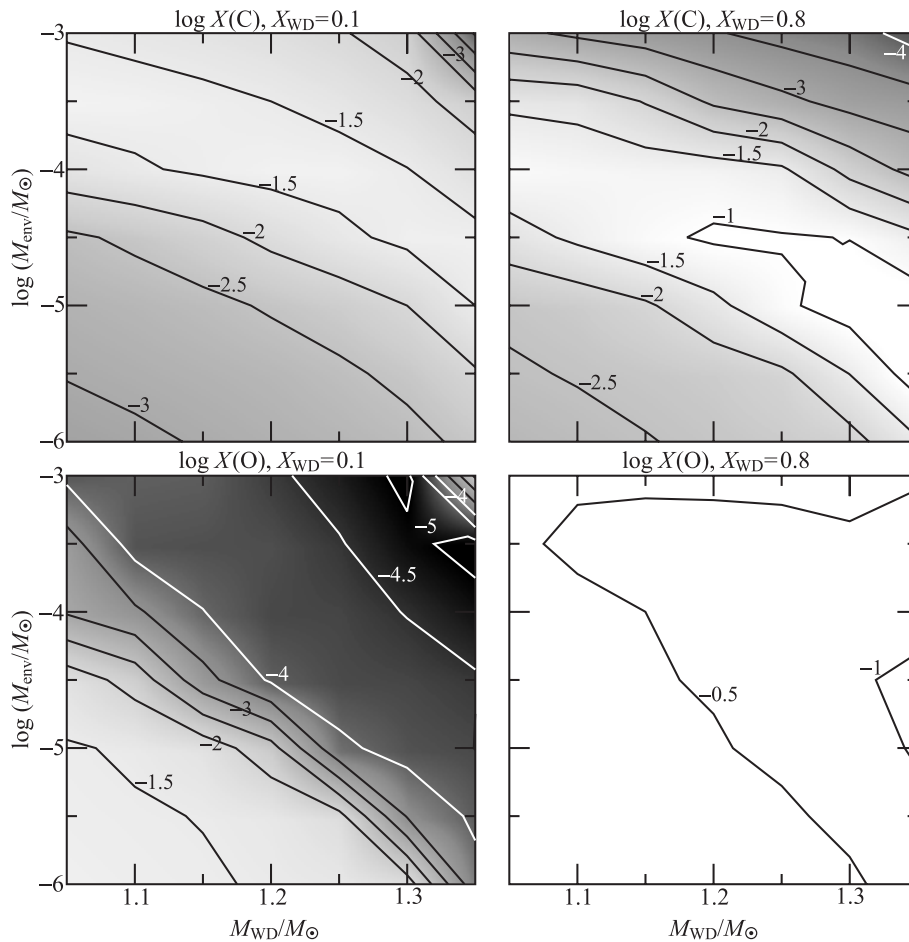
FIG. 18.—Contours of the abundances of carbon and oxygen in the logarithmic scale for case A and C

$T_{\rm peak} \sim 2$–3×10^8 K, which is inconsistent with the above result. Thus, there is no $(M_{\rm WD}, M_{\rm env})$ model that explains the abundance estimates by Saizar et al. (1992) within reasonable observational errors.

The V838 Her ejecta also shows a rather low metallicity estimate ($Z \simeq 0.09$), which again corresponds to case A. The abundance features of the ejected shell, i.e., the low oxygen and high sulfur, are well reproduced in our results for $T_{\rm peak} \sim 2$–3×10^8 K (Figs. 18 and 19). Hence, the low metallicity for this case implies the presence of a real dispersion in metallicity among the observed nova ejecta.

5. COMPARISON WITH OBSERVATIONS

In this section, we discuss which $(M_{\rm WD}, M_{\rm env})$ models best match the recent ONeMg nova observations from the nucleosynthetic point of view, using the results of case B ($X_{\rm WD} = 0.4$). For V838 Her, however, those of case A ($X_{\rm WD} = 0.1$) are used (§ 4.3). The abundances for QU Vul by Saizar et al. (1992) and V1370 Aql are not discussed in this section, since they are not reproduced in our models (§ 4.3).

Figure 21 shows the models that are in agreement with the abundance estimates for recent ONeMg novae to within a factor of 3 for V693 CrA (Vanlandingham et al. 1997; *triangles*), V351 Pup (Saizar et al. 1996; *asterisks*), and V1974 Cyg (Austin et al. 1996; *stars*) and a factor of 5 for QU Vul (Andreä et al. 1994; *circles*) and V838 Her (Vanlandingham et al. 1997; *squares*). The thick symbol for each nova is the best model, whose ratio to its observation

is shown in Figure 22. Interestingly, at least four events (V693 CrA, QU Vul, V838 Her, and V1974 Cyg) are well explained by the models with $\simeq 1.1\ M_\odot$, which is near the lower limit for ONeMg cores (Nomoto 1984). This is in contrast to the mass range used by PSTWS95 and STWS98, 1.25–1.35 $M_\odot$, which is near the upper bound for ONeMg cores. Table 5 shows the estimated ejecta masses of QU Vul (Taylor et al. 1987; Greenhouse et al. 1988; Saizar et al. 1992), V351 Pup (Saizar et al. 1996), V838 Her (Woodward et al. 1992; Vanlandingham et al. 1996), and V1974 Cyg (Pavelin et al. 1993; Shore et al. 1993; Woodward et al. 1997) from observations. These significantly high ejecta masses compared with theoretical estimates are reasonably explained by our nucleosynthesis results if we assume that almost all the envelope is eventually blown off. In addition, for the models with $M_{\rm env} \gtrsim 10^{-4}\ M_\odot$, the expansion velocities exceed $v_{\rm esc}$ and obtain $v_{\rm ej} \gtrsim 1000$ km s^{-1} (Figs. 6 and 16), which are in good agreement with observations. Note that the abundances of carbon and nitrogen by our results are also in good agreement with those by observations, regardless of their uncertainties (§ 3). This is a consequence that these novae are well explained by the models with $\tau \lesssim 1000$ s where the uncertainties (caused by the depletion of ^{15}N) may be small (§ 4.2.2).

5.1. V693 CrA

The high oxygen abundance (~ 0.1–0.2 by mass) in the V693 CrA ejecta (Williams et al. 1985; Andreä et al. 1994;
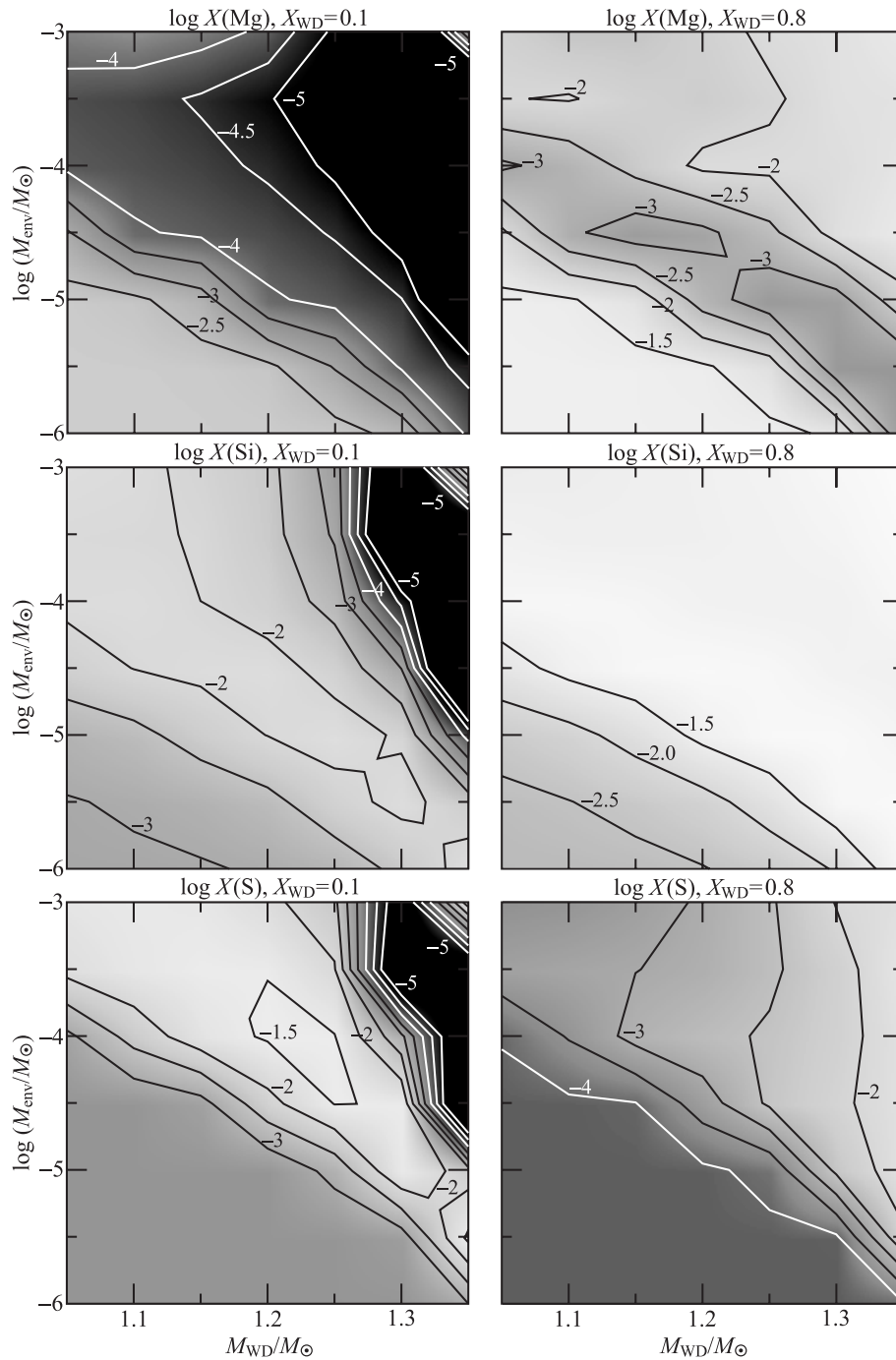
Fig. 19.—Same as Fig. 18, but for magnesium, silicon, and sulfur

Vanlandingham et al. 1997) implies that it was an event with $T_{\rm peak} \lesssim 2 \times 10^8$ K or with $M_{\rm WD} \lesssim 1.15\ M_\odot$ (§ 4.2.3). The low magnesium and high silicon abundances found by Vanlandingham et al. (1997) suggest that the cooling time-scale was $\lesssim 1000$ s (§§ 4.2.5 and 4.2.6). On the other hand, Williams et al. (1985) and Andreä et al. (1994) present somewhat higher magnesium and lower silicon abundances. We compare our results with the abundance estimates by Vanlandingham et al. (1997), since others used the overexposed spectrum as pointed out by Andreä et al. (1994). As a result, the model $(M_{\rm WD}/M_\odot, M_{\rm env}/M_\odot) = (1.05, 10^{-3})$ (case B) is in good agreement with the observation to within a factor of 3 (Figs. 21 and 22).

5.2. QU Vul

The high abundance of sulfur implies that the nova reached temperature as high as $T_{\rm peak} \gtrsim 3 \times 10^8$ K (Figs. 6 and 14). Furthermore, the abundance of oxygen despite such a high temperature suggests that the white dwarf mass was $\lesssim 1.15\ M_\odot$ (§ 4.2.3). Our results are in agreement with the observational estimates to within a factor of 5 for the models $(M_{\rm WD}/M_\odot, M_{\rm env}/M_\odot) = (1.05–1.1, 10^{-3.5}$ to $10^{-3})$ (case B). These high envelope masses are in good agreement with the observational estimates of the nova ejecta (Table 5). Note that the high abundances of both oxygen and sulfur were not explained by previous hydrodynamic studies, with much smaller envelope masses.
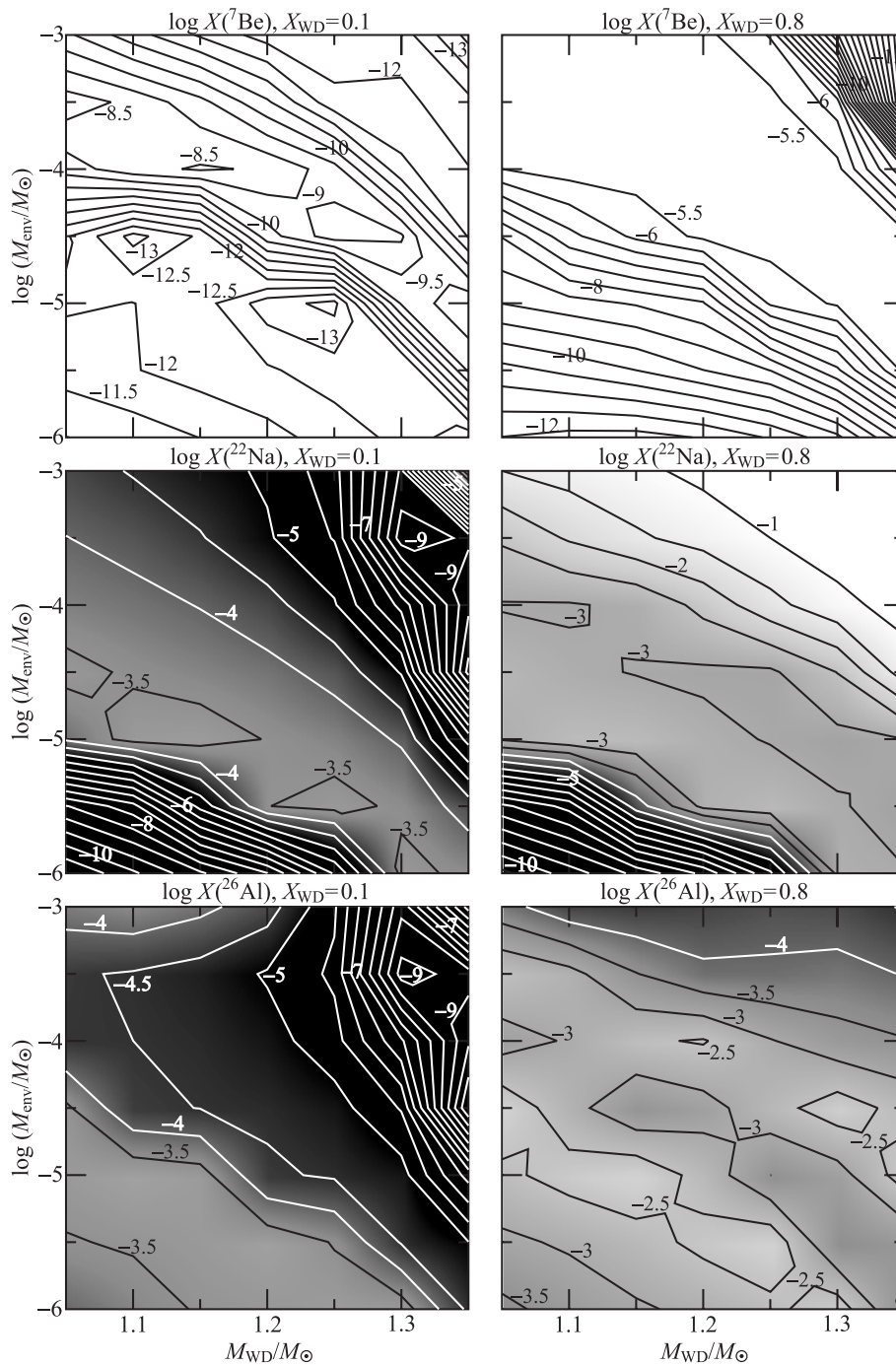
FIG. 20.—Same as Fig. 18, but for ^{7}Be, ^{22}Na, and ^{26}Al

5.3. *V351 Pup*

The ejected shell of V351 Pup shows the high oxygen and low silicon abundances (Saizar et al. 1996). This feature is well explained with the low-temperature models of $T_{peak} \lesssim 2 \times 10^8$ K (Figs. 6, 10, and 13). Our results are in good agreement with the observational estimates to within a factor of 3 for the models $(M_{WD}/M_\odot,\ M_{env}/M_\odot) = (1.05–1.1, 10^{-5.5}$ to $10^{-5}), (1.15–1.2, 10^{-6}$ to $10^{-5.5})$ and are the best for $(1.25, 10^{-6})$ (case B). In such low-temperature models, magnesium must be abundant (§ 4.2.5), though it is not presented in Saizar et al. (1996). The above low envelope

masses may be due to mass accreting at a high rate from a giant companion, which is also suggested by the optical spectral analysis (Saizar et al. 1996). The estimated ejecta mass, $2 \times 10^{-7}\ M_\odot$ (Table 5), implies that this nova occurred in a white dwarf as massive as $M_{WD} \gtrsim 1.25\ M_\odot$.

5.4. *V838 Her*

The low oxygen and high sulfur abundances in the V838 Her ejecta are the prominent features in the low-metallicity models (case A) with $T_{peak} \sim 2.5–3 \times 10^8$ K (§ 4.3). In addition, the ratios C/N ~ 1 and C/O $\gtrsim 1$ suggest that the
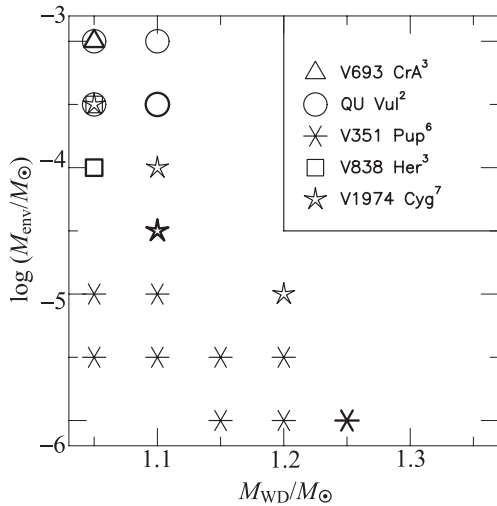
FIG. 21.—(M_{WD}, M_{env}) sequences that are in agreement with recent ONeMg novae, within the factor of 3 for V693 CrA (*triangles*), V351 Pup (*asterisks*), and V1974 Cyg (*stars*), and of five for QU Vul (*circles*) and V838 Her (*squares*). The thick signs are the best sequences in our results.

cooling timescale was ~ 1000 s (§§ 4.2.2 and 4.2.3). Thus, the nova may have occurred at low M_{WD} and high M_{env} (Fig. 15). Our results are in agreement with the observational estimates to within a factor of 5 for the model $(M_{WD}/M_\odot, M_{env}/M_\odot) = (1.05, 10^{-4} \text{ to } 10^{-3.5})$.
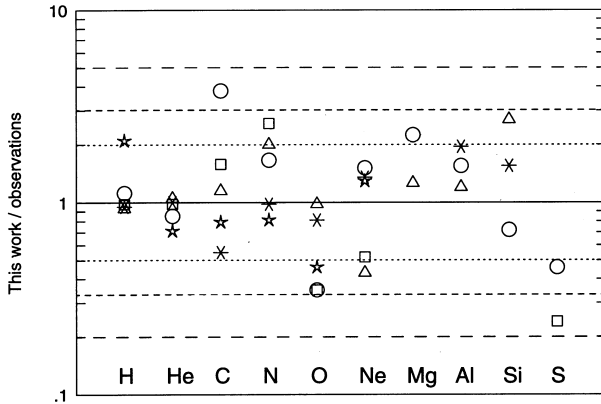

FIG. 22.—Ratios of our results to observational abundance estimates. The symbols are the same as Fig. 20.

5.5. V1974 Cyg

Unfortunately, the abundances of elements heavier than neon are not presented in Austin et al. (1996), because of a lack of these lines. The high oxygen abundance suggests that the peak temperature was $\lesssim 2 \times 10^8$ K or that the white dwarf mass was $\lesssim 1.15\ M_\odot$ (§ 4.2.3). In addition, the ratio C/N ~ 1 implies that the cooling timescale was ~ 1000 s (§ 4.2.2). Our results are in good agreement with the observational estimates to within a factor of 3 for the models $(M_{WD}/M_\odot, M_{env}/M_\odot) = (1.05, 10^{-3.5})$, $(1.1, 10^{-4})$, and $(1.2, 10^{-5})$ and are the best for $(1.1, 10^{-4.5})$ (case B; N0535B, N1040B, N2050B, and N1045B). They are in reasonable agreement with the estimated mass of the ejecta $\gtrsim 5 \times 10^{-5}\ M_\odot$ (Table 5). Their white dwarf masses are also in agreement with the estimates from observations ~ 0.75–$1.1\ M_\odot$ (Paresce et al. 1995; Retter et al. 1997) but are smaller than $\sim 1.25\ M_\odot$ (Krautter et al. 1996). The observation shows a factor of 2 lower hydrogen abundance than our result (Fig. 22). This might be due to the subsequent steady hydrogen burning on the white dwarf as pointed out by Krautter et al. (1996). Hayward et al. (1996) have derived the neon and magnesium abundances relative to solar values from a mid-infrared observation. If their ratio Ne/Mg ~ 30 is adopted, the abundance of magnesium would be $\sim 3 \times 10^{-3}$. It favors a relatively high envelope mass model (Fig. 12). As a result, N1040B would be the best in this case. A recent near-infrared measurement has shown the presence of the lines of phosphorus and chlorine together with sulfur in the V1974 Cyg ejecta (Wagner & DePoy 1996). This suggests that V1974 Cyg experienced $T_{peak} \gtrsim 3 \times 10^8$ K. In this case, the higher M_{env} models are also favorable. In addition, the ejection velocity in N1040B is $\simeq 1800$ km s^{-1} being good agreement with observations ($\simeq 2300$ km s^{-1}; Gehrz et al. 1998), while that in N1045B is $\simeq 190$ km s^{-1}. Obviously, further analysis of heavy elements is needed to constrain the parameters (M_{WD}, M_{env}) for V1974 Cyg.

6. PRODUCTION OF THE RADIOACTIVE ISOTOPES

In this section, we discuss the possibilities of detecting the γ-ray emitters ^{7}Be and ^{22}Na and the contribution to the Galactic ^{26}Al from ONeMg novae, based on our nucleosynthesis results in ONeMg novae. Figure 23 shows the total masses of ^{7}Be, ^{22}Na, and ^{26}Al produced per event for $X_{WD} = 0.4$ (case B). As seen in this figure, the models with

TABLE 5

Ejected Masses of Recent ONeMg Novae

Nova	$M_{ej}/M_\odot$	Observations	Ref.
QU Vul	8×10^{-4}	Radio emission	1
QU Vul	$\geq 9 \times 10^{-4}$	Infrared emission	2
QU Vul	0.2–1.5×10^{-4}	Multiwavelength study	3
V351 Pup	1×10^{-7}	Multiwavelength study	4
V838 Her	6.4–9×10^{-5}	Infrared emission	5
V838 Her	1.8×10^{-4}	Optical and UV emission	6
V1974 Cyg......	$\geq 7 \times 10^{-5}$	Radio emission	7
V1974 Cyg......	1–$4 \times 10^{-4} \times Y^{-1/2}$ [a]	UV emission	8
V1974 Cyg......	2–5×10^{-4}	Infrared emission	9

[a] Y is the enhancement factor for the helium abundance.

REFERENCES.—(1) Taylor et al. 1987; (2) Greenhouse et al. 1988; (3) Saizar et al. 1992; (4) Saizar et al. 1996; (5) Woodward et al. 1992; (6) Vanlandingham et al. 1996; (7) Pavelin et al. 1993; (8) Shore et al. 1993; (9) Woodward et al. 1997.
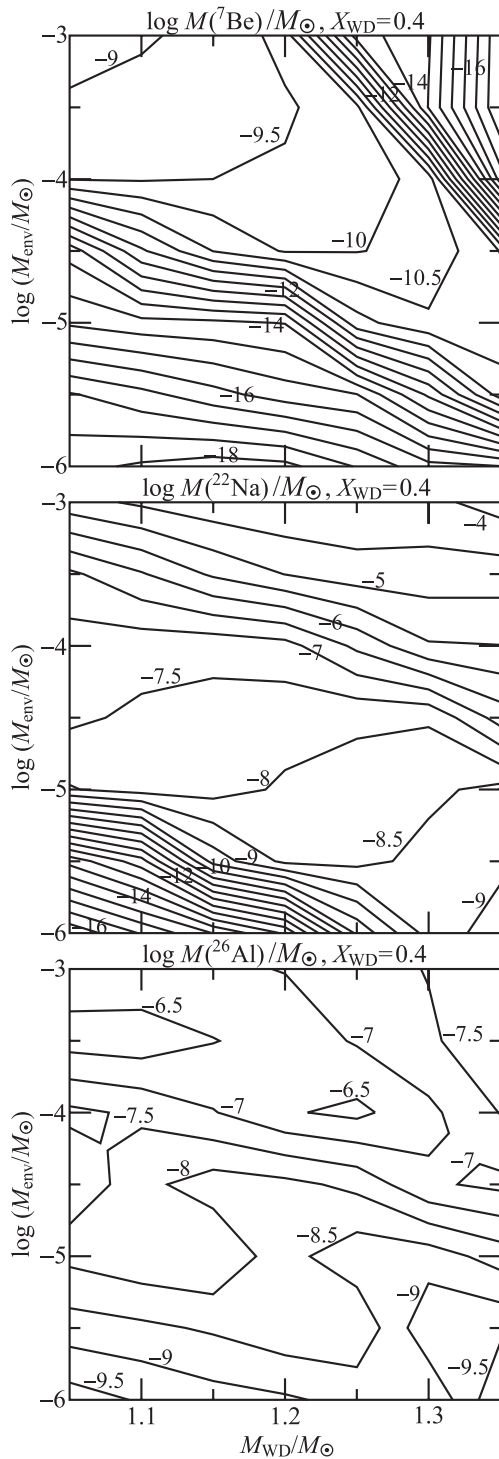
FIG. 23.—Contours of the masses of ^{7}Be, ^{22}Na, and ^{26}Al per event in the logarithmic scale (case B).

$M_{WD} \simeq 1.1\ M_\odot$ with $M_{env} \gtrsim 10^{-4}\ M_\odot$, which are in good agreement with most of observations (§ 5), produce significant amounts of these isotopes. In the rest of this section, all of the envelope is assumed to be eventually blown off.

6.1. Gamma-Ray Emission from ^{7}Be Electron Captures

Classical novae might be possible sites for the ^{7}Li production (the electron-capture products of ^{7}Be) in the solar neighborhood (Starrfield et al. 1978; D'Antona & Mat-

teucci 1991; Wanajo, Ishimaru, & Kajino 1998). Recently, some works claim that they cannot be the major contributors (Matteucci, D'Antona, & Timmes 1995; JH98). Nevertheless, the γ-rays (at 478 KeV) from the ^{7}Be electron capture would be detectable by *CGRO* or *INTEGRAL* (Hernanz et al. 1996; José & Hernanz 1998; Gómez-Gomar et al. 1998).

The γ-ray line flux from the ^{7}Be electron capture is estimated as

$$F(^7\text{Be}) \sim 4 \times 10^{-5}\ \text{cm}^{-2}\ \text{s}^{-1}$$

$$\times \left[\frac{X(^7\text{Be})M_{env}}{5 \times 10^{-9}\ M_\odot} \right] \left(\frac{d}{3\ \text{kpc}} \right)^{-2} e^{-t/\tau(^7\text{Be})},$$

where d is the distance of the nova system from the sun. For the *CGRO* sensitivity (a few $10^{-5}\ \text{cm}^2\ \text{s}^{-1}$) and a typical distance ($d \sim 3$ kpc), a mass of ^{7}Be $\sim 5 \times 10^{-9}\ M_\odot$ per event is required for it to be detected. The mass of ^{7}Be per event in our model is over 5–10 times smaller than required (Fig. 23). However, an ONeMg nova will be a promising target in ^{7}Be γ-rays for *INTEGRAL* in the near future. Note that CO novae may produce about 10 times higher ^{7}Be than ONeMg novae (JH98; Wanajo et al. 1998).

6.2. Gamma-Ray Emission from ^{22}Na Decays

There has been increasing expectations that an ONeMg nova might be the first stellar object for the detection of the γ-ray emitter ^{22}Na (Weiss & Truran 1990; Starrfield et al. 1993; Coc et al. 1995; PSTWS95; Wanajo 1997a, 1997b; STWS98; JH98; Gómez-Gomar et al. 1998). Nevertheless, no positive detection has been reported by COMPTEL on board *CGRO* for the recent ONeMg novae, V351 Pup, V838 Her, and V1974 Cyg (Iyudin et al. 1995).

As seen in Figure 23, the total mass of ^{22}Na per event (case B) is significantly high in the models $M_{env} \gtrsim 10^{-4}\ M_\odot$. The γ-ray line flux from the β^+-decay of ^{22}Na is estimated as

$$F(^{22}\text{Na}) \sim 4 \times 10^{-5}\ \text{cm}^{-2}\ \text{s}^{-1}$$

$$\times \left[\frac{X(^{22}\text{Na})M_{env}}{1 \times 10^{-7}\ M_\odot} \right] \left(\frac{d}{3\ \text{kpc}} \right)^{-2} e^{-t/\tau(^{22}\text{Na})}.$$

For the *CGRO* sensitivity and a typical distance (~ 3 kpc), a mass of ^{22}Na $\sim 10^{-7}\ M_\odot$ per event is required. This corresponds to an envelope mass of $\sim 10^{-4}\ M_\odot$ (Fig. 23). Table 6 shows the distances, the masses of ^{22}Na per event from our results (for the best fitted models, see § 5), the expected initial γ-ray line fluxes at 1.275 MeV, and the upper limits to the COMPTEL observations (Iyudin et al. 1995) for V693 CrA, QU Vul, V351 Pup, V838 Her, and V1974 Cyg. V1370 Aql is omitted here, not explained by any (M_{WD}, M_{env}) models as discussed in § 5. V693 CrA and QU Vul may have emitted the γ-rays as high as $\sim 5 \times 10^{-4}\ \text{cm}^{-2}\text{s}^{-1}$. However, their fluxes have decreased to, respectively, 6×10^{-6} and $1 \times 10^{-5}\ \text{cm}^2\ \text{s}^{-1}$ at present, and will decrease to 3×10^{-6} and $5 \times 10^{-6}\ \text{cm}^2\ \text{s}^{-1}$ at the launch of *INTEGRAL* (~ 2001?). In contrast to the above two novae, V351 Pup and V838 Her may have yielded much lower γ-ray fluxes that are consistent with the upper limits by COMPTEL. The envelope mass of V351 Pup might be $\lesssim 10^{-5}\ M_\odot$ (§ 5.3), so little ^{22}Na may have been produced. Although V838 Her may have obtained a massive envelope such as $\sim 10^{-4}\ M_\odot$ (§ 5.4), the cooling timescale was so long owing to the low metallicity ($\sim 10^4$ s) that little ^{22}Na

TABLE 6

^{22}Na Production in ONeMg Novae

Nova	Year	d (kpc)	$XM_{env}/M_\odot$	F_0[a] (cm^{-2} s^{-1})	F_{up}[b] (cm^{-2} s^{-1})
V693 CrA.......	1981	11.8	2.0×10^{-5}	5.5×10^{-4}	
QU Vul	1984	2.8	8.9×10^{-7}	4.4×10^{-4}	
V351 Pup	1991	3.5	4.0×10^{-11}	1.3×10^{-8}	5.5×10^{-5}
V838 Her	1991	3.4	1.9×10^{-8}	6.3×10^{-6}	3.3×10^{-5}
V1974 Cyg......	1992	1.8	2.5×10^{-8}	3.0×10^{-5}	2.3×10^{-5}

[a] Initial flux by this work (best sequence).
[b] Upper limit by Iyudin et al. 1995.

survived. The γ-ray flux of the ^{22}Na decay from V1974 Cyg may have been near the sensitivity limit to COMPTEL, with the abundance in the best model (§ 5.5) and a distance of ~ 1.8 kpc (Chochol et al. 1997). Thus, if the ejected mass was as high as a few 10^{-4} $M_\odot$, our model would indeed have produced observable ^{22}Na (or the estimated distance is too short).

It seems that at least four ONeMg novae (V693 CrA, QU Vul, V838 Her, and V1974 Cyg) in the past 20 years have produced sufficient ^{22}Na for the high sensitivity of *INTEGRAL* (~ 4–5×10^{-6} cm^2 s^{-1}). The next ONeMg nova in the first decade of the 21st century will be a promising candidate for detecting the γ-ray emitter ^{22}Na.

6.3. *Galactic* ^{26}Al *Production*

Since its discovery by *HEAO 3* (Mahoney et al. 1984), many studies have been carried out to explain the presence of ~ 1–3 $M_\odot$ of ^{26}Al in the Galaxy. In particular, ONeMg novae have been considered to be a promising stellar site for the ^{26}Al production (Weiss & Truran 1990; Nofar et al. 1991; Starrfield et al. 1993; Coc et al. 1995; PSTWS95; Kolb & Politano 1997; José et al. 1997; STWS98; JH98), as well as asymptotic giant branch stars (Forestini, Paulus, & Arnould 1991), Wolf-Rayet stars (Prantzos & Cassé 1986; Meynet et al. 1997), and Type II supernovae (Walter & Maeder 1989; Prantzos 1993; Timmes et al. 1995). However, the detailed observations of γ-ray lines at 1.8 MeV by COMPTEL (Diehl et al. 1994, 1995) have shown that the Galactic ^{26}Al originates from the youngest stellar population associated with the spiral arms and the local groups (Prantzos & Diehl 1996; Prantzos 1996). This may imply that the major sources of the Galactic ^{26}Al are Type II supernovae or Wolf-Rayet stars.

The mass of ^{26}Al per event is up to $\sim 3 \times 10^{-7}$ $M_\odot$ in the models $M_{env} \gtrsim 10^{-4}$ $M_\odot$ (Fig. 23). The upper limit to the Galactic ^{26}Al from ONeMg novae is thus estimated as

$$M(^{26}Al) \sim 3 \ M_\odot \left(\frac{R_{nova}}{40 \ yr^{-1}}\right)\left(\frac{f_{ONeMg}}{0.25}\right)\left[\frac{X(^{26}Al)M_{env}}{3 \times 10^{-7}}\right],$$

where R_{nova} is the nova rate in the Galaxy and f_{ONeMg} is the fraction of ONeMg novae. This is in good agreement with the estimate from the *CGRO* results. If ONeMg novae are not the major contributors to the Galactic ^{26}Al, its typical mass per ONeMg nova event must be somewhat smaller than the above value. There are some uncertainties in the Galactic nova rates (Yungelson, Livio, & Tutukov 1997; Shafter 1997; Hatano et al. 1997) and the fraction of ONeMg novae (Ritter et al. 1991; Livio & Truran 1994). However, these uncertainties may be much smaller (by a factor of ~ 2)

than those in the ^{26}Al yields (about 2 orders of magnitude, as can be seen in Fig. 23). The *INTEGRAL* survey on the diffuse component of the Galactic ^{26}Al, together with a search of ^{22}Na from an individual ONeMg nova, will impose a severe constraint on the current nova models.

7. CONCLUSIONS

In this paper we have examined nucleosynthesis in ONeMg novae with wide ranges of three parameters, i.e., the white dwarf mass ($M_{WD} = 1.05$–1.35 $M_\odot$), the envelope mass ($M_{env} = 10^{-6}$ to 10^{-3} $M_\odot$), and the initial metallicity ($X_{WD} = 0.1$–0.8). We used a quasi-analytic nova model with a one-zone envelope, coupled with an updated nuclear reaction network code. Except for several fragile isotopes, our nucleosynthesis results are in good agreement with those of previous hydrodynamic calculations.

We have found that the explosion is more violent in a lower M_{WD} model among those with the same peak temperature because of its smaller gravitational potential. There exists a critical cooling timescale (~ 1000 s) at which the energy generation by the β^+-decay of ^{14}O and ^{15}O plays a crucial role to the envelope expansion. For the models with $\tau \lesssim 1000$ s, the nucleosynthesis results significantly deviate from those expected in steady nuclear flows (e.g., the CNO and Ne–Na cycle). These models also obtain high ejection velocities ($\gtrsim 1000$ km s^{-1}), which are in good agreement with recent observations.

There are a few characteristic trends for the abundances in the M_{WD}-M_{env} space as follows (case B).

1. The abundances of oxygen, neon, phosphorus, and sulfur (and ^{7}Be) are clearly correlated to the peak temperatures, although those of oxygen and sulfur are also dependent of the cooling timescales. The abundance of oxygen is always abundant in the models $M_{WD} \lesssim 1.15$ $M_\odot$. The heavier elements than sulfur show no significant enrichment in the models with $T_{peak} \lesssim 4 \times 10^8$ K.

2. The abundances of carbon, fluorine, sodium, and magnesium (and ^{22}Na, ^{26}Al) are clearly correlated to the cooling timescales. The abundance of ^{22}Na is significantly high in the models with $\tau \lesssim 100$ s. On the other hand, that of ^{26}Al shows double peaks in the M_{WD}-M_{env} space.

3. The abundances of nitrogen, aluminum, and silicon are not significantly changed in the M_{WD}-M_{env} space, although those are weakly dependent of the cooling timescales.

The initial metallicity X_{WD}, as well as M_{WD} and M_{env}, is a crucial parameter to the nucleosynthesis results. For smaller X_{WD}, the explosion is less violent and thus the

cooling timescale is longer, because of the smaller nuclear fuel. As a result, the models with low X_{WD} (case A) produce more sulfur but less oxygen than those with high X_{WD} (cases A and B). The former case is unfavorable for the production of ^{7}Be, ^{22}Na, and ^{26}Al.

Comparison of our nucleosynthesis results with observational abundance estimates enables us to constrain the model parameters (M_{WD}, M_{env}) for the observed ONeMg novae. We have found that the white dwarf masses of at least four of the observed six ONeMg novae are as low as $\simeq 1.1\ M_\odot$. This is significantly smaller than the prediction of $M_{WD} \sim 1.25$–$1.35\ M_\odot$ obtained by previous hydrodynamic studies. On the other hand, our results suggest that their envelope masses were $\gtrsim 10^{-4}\ M_\odot$, consistent with the observational estimates of their ejected masses. In addition, the observed fast ejection velocities for these novae ($\gtrsim 1000$ km s^{-1}) are also obtained in those models. There remains a discrepancy between these high ejected masses and those estimated by previous hydrodynamic studies. However, a low-mass white dwarf ($M_{WD} \simeq 1.1\ M_\odot$) may be able to accumulate such a massive envelope with a small mass accretion rate and a low surface temperature (Starrfield et al. 1998).

Our results also show that the models $M_{WD} \simeq 1.1\ M_\odot$ with $M_{env} \gtrsim 10^{-4}\ M_\odot$, which are possible explanations for most of the observed ONeMg novae, produce significant amounts of ^{7}Be, ^{22}Na, and ^{26}Al.

1. The γ-ray line flux from the ^{7}Be electron capture is too weak to be detected with the *CGRO* sensitivity for the typical distance from the sun. However, a nearby ONeMg nova could emit the γ-rays detectable by *INTEGRAL* in the near future.

2. The mass of ^{22}Na per event is significantly high in the models $M_{env} \gtrsim 10^{-4}\ M_\odot$. V1974 Cyg may have produced an interesting amount of ^{22}Na, which is near the upper limit to the COMPTEL sensitivity. Furthermore, we suggest that

at least four ONeMg novae in the past twenty years have produced enough ^{22}Na to the *INTEGRAL* sensitivity. The next ONeMg nova will be a promising target for the detection of the γ-ray emitter ^{22}Na.

3. The mass of ^{26}Al per event is also significantly high in the models $M_{env} \gtrsim 10^{-4}\ M_\odot$. The mass of the Galactic ^{26}Al, which originates from ONeMg novae is estimated to be $\lesssim 3\ M_\odot$, being consistent to the COMPTEL result. They may not be, however, major contributors according to the γ-ray survey at 1.8 MeV by COMPTEL. The γ-ray line survey by *INTEGRAL* will significantly constrain the ranges of (M_{WD}, M_{env}) for ONeMg novae.

REFERENCES

Anders, E., & Grevesse, N. 1989, Geochim. Cosmochim. Acta, 53, 197
Andreä, J., Drechsel, H., & Starrfield, S. 1994, A&A, 291, 869
Austin, S. J., Wagner, R. M., Starrfield, S., Shore, S. N., Sonneborn, G., & Bertram, R. 1996, AJ, 111, 869
Boffin, H. M. J., Paulus, G., Arnould, M., & Mowlavi, N. 1993, A&A, 279, 173
Caughlan, G. R., & Fowler, W. A. 1988, At. Data Nucl. Data Tables, 40
Champagne, A. E., Brown, B. A., & Sherr, R. 1993, Nucl. Phys. A, 556, 123
Champagne, A. E., Cella, C. H., Kouzes, R. T., Lowry, M. M., Magnus, P. V., Smith, M. S., & Mao, Z. Q. 1988, Nucl. Phys. A, 487, 433
Chochol, D., Grygar, J., Pribulla, T., Komžík, R., Hric, L., & Elkin, V. 1997, A&A, 318, 908
Coc, A., Mochkovitch, R., Oberto, Y., Thibaud, J. P., & Vangioni-Flam, E. 1995, A&A, 299, 479
D'Antona, F., & Matteucci, F. 1991, A&A, 248, 62
Diehl, R., et al. 1994, ApJS, 92, 429
———. 1995, A&A, 298, 445
Forestini, M., Paulus, G., & Arnould, M. 1991, A&A, 252, 597
Fujimoto, M. Y. 1982a, ApJ, 257, 752
———. 1982b, ApJ, 257, 767
Gehrz, R. G., Truran, J. W., Williams, R. E., & Starrfield, S. 1998, PASP, 110, 3
Gehrz, R. D., et al. 1994, ApJ, 421, 762
Glasner, S. A., Livne, E., & Truran, J. W. 1997, ApJ, 475, 754
Gómez-Gomar, J., Hernanz, M., José, J., & Isern, J. 1998, MNRAS, 296, 913
Greenhouse, M. A., Grasdalen, G. L., Hayward, T. L., Gehrz, R. D., & Jones, T. J. 1988, AJ, 95, 172
Hamada, T., & Salpeter, E. E. 1961, ApJ, 134, 683
Hashimoto, M., Iwamoto, K., & Nomoto, K. 1993, ApJ, 414, 105
Hatano, K., Branch, D., Fisher, A., & Starrfield, S. 1997, MNRAS, 290, 113
Hayward, T. L., et al. 1996, ApJ, 469, 854
Hernanz, M., José, J., Coc, A., & Isern, J. 1996, ApJ, 465, 27
Herndl, H., Görres, J., Wiescher, M., Brown, B. A., & van Wormer, L. 1995, Phys. Rev. C, 52, 1078

Hillebrandt, W., & Thielemann, F.-K. 1982, ApJ, 255, 617
Iben, I., Jr., Fujimoto, M. Y., & MacDonald, J. 1991, ApJ, 375, 27
Iben, I., Jr., & Tutukov, A. V. 1985, ApJS, 58, 661
Ichimaru, S., & Kitamura, H. 1994, in Proc. Int. Semi. on Elementary Processes in Dense Plasmas, ed. S. Ichimaru & S. Ogata (Addison-Wesley), 113
Iglesias, C. A., & Rogers, F. J. 1993, ApJ, 412, 752
Iliadis, C., Buchmann, L., Endt, P. M., Herndl, H., & Wiescher, M. 1996, Phys. Rev. C, 53, 475
Iyudin, A. F., et al. 1995, A&A, 300, 422
José, J., & Hernanz, M. 1998, ApJ, 494, 680 (JH98)
José, J., Hernanz, M., & Coc, A. 1997, ApJ, 479, 55
Kercek, A., Hillebrandt, W., & Truran, J. W. 1998a, A&A, 337, 379
———. 1998b, A&A, submitted
Kolb, U., & Politano, M. 1997, A&A, 319, 909
Kovetz, A., & Prialnik, D. 1997, ApJ, 477, 356
Krautter, J., Ögelman, H., Starrfield, S., Wichmann, R., & Pfeffermann, E. 1996, ApJ, 456, 788
Kubono, S., et al. 1994, Z. Phys. A, 348, 59
———. 1997, Nucl. Phys. A, 621, 195
Kutter, G. S., & Sparks, W. M. 1987, ApJ, 321, 386
Livio, M., & Truran, J. W. 1994, ApJ, 425, 797
MacDonald, J. 1983, ApJ, 267, 732
Mahoney, W. A., Ling, J. C., Wheaton, W. A., & Jacobson, A. S. 1984, ApJ, 286, 578
Matteucci, F., D'Antona, F., & Timmes, F. X. 1995, A&A, 303, 460
Meynet, G., Arnould, M., Prantzos, N., & Paulus, G. 1997, A&A, 320, 460
Nofar, I., Shaviv, G., & Starrfield, S. 1991, ApJ, 369, 440
Nomoto, K. 1984, ApJ, 277, 291
———. 1987, ApJ, 322, 206
Nomoto, K., & Hashimoto, M. 1988, Phys. Rep., 163, 13
Paresce, F., Livio, M., Hack, W., & Korista, K. 1995, A&A, 299, 823
Pavelin, P. E., Davis, R. J., Morrison, L. V., Bode, M. F., & Ivison, R. J. 1993, Nature, 363, 424

Politano, M., Starrfield, S., Truran, J. W., Weiss, A., & Sparks, W. M. 1995, ApJ, 448, 807 (PSTWS95)
Prantzos, N. 1993, ApJ, 405, L55
———. 1996, A&AS, 120, 303
Prantzos, N., & Cassé, M. 1986, ApJ, 307, 324
Prantzos, N., & Diehl, R. 1996, Phys. Rep., 267, 1
Prialnik, D., & Kovetz, A. 1984, ApJ, 281, 367
———. 1995, ApJ, 445, 789
Retter, A., Leibowitz, E. M., & Ofek, E. O. 1997, MNRAS, 286, 745
Ritossa, C., García, E.-B., & Iben, I. 1996, ApJ, 460, 489
Ritter, H., Politano, M., Livio, M., & Webbink, R. F. 1991, ApJ, 376, 177
Saizar, P., Pachoulakis, I., Shore, S. N., Starrfield, S., Williams, R. E., Rothschild, E., & Sonneborn, G. 1996, MNRAS, 279, 280
Saizar, P., et al. 1992, ApJ, 398, 651
Schmidt, S., et al. 1995, Nucl. Phys. A, 591, 227
Shafter, A. W. 1997, ApJ, 487, 226
Shields, G. A. 1996, ApJ, 461, 9
Shore, S. N., Sonneborn, G., Starrfield, S., Gonzalez-Riestra, R., & Ake, T. B. 1993, AJ, 106, 2408
Sion, E. M., Cheng, F. H., Sparks, W. M., Szkody, P., Huang, M., & Hubeny, I. 1997, ApJ, 480, 17
Snijders, M. A. J., Batt, T. J., Roche, P. F., Seaton, M. J., Morton, D. C., Spoelstra, T. A. T., & Blades, J. C. 1987, MNRAS, 228, 329
Starrfield, S., Sparks, W. M., & Shaviv, G. 1988, ApJ, 325, 35
Starrfield, S., Truran, J. W., Politano, M., Sparks, W. M., Nofar, I., & Shaviv, G. 1993, Phys. Rep., 227, 223
Starrfield, S., Truran, J. W., & Sparks, W. M. 1978, ApJ, 226, 186
Starrfield, S., Truran, J. W., Wiescher, M. C., & Sparks, W. M. 1998, MNRAS, 296, 502 (STWS98)
Sugimoto, D., & Fujimoto, M. Y. 1978, PASJ, 30, 467
Taylor, A. R., Seaquist, E. R., Hollis, J. M., & Pottasch, S. R. 1987, A&A, 183, 38
Timmernamm, R., Becker, H. W., Rolfs, C., Schröder, U., & Trautvetter, H. P. 1988, Nucl. Phys. A, 477, 105
Timmes, F. X., Woosley, S. E., Hartmann, D. H., & Hoffman, R. D. 1995, ApJ, 449, 204

Truran, J. W. 1982, in Essays in Nuclear Astrophysics, ed. C. A. Barnes, D. D. Clayton, & D. N. Schramm (Cambridge: Cambridge Univ. Press), 467
Truran, J. W., Starrfield, S., Strittmatter, P. A., Wyatt, S. P., & Sparks, W. M. 1977, ApJ, 211, 539
Truran, J. W., Thielemann, F.-K., & Arnould, M. 1987, in Nuclear Astrophysics, ed. D. Hillebrandt (Berlin: Springer), 91
Vanlandingham, K. M., Starrfield, S., & Shore, S. N. 1997, MNRAS, 290, 87
Vanlandingham, K. M., Starrfield, S., Wagner, R. M., Shore, S. N., & Sonneborn, G. 1996, MNRAS, 282, 563
van Wormer, L., Görres, J., Iliadis, C., Wiescher, M., & Thielemann, F.-K. 1994, ApJ, 432, 326
Wagner, R. M., & DePoy, D. L. 1996, A&A, 218, 123
Walter, R., & Maeder, A. 1989, A&A, 218, 123
Wanajo, S., Ishimaru, Y., & Kajino, T. 1998, in Origin of Matter and Evolution of Galaxies 97, ed. S. Kubono, T. Kajino, K. Nomoto, & I. Tanihata (Singapore: World), 262
Wanajo, S., Nomoto, K., Hashimoto, M., Kajino, T., & Kubono, S. 1997a, Nucl. Phys. A, 616, 91
Wanajo, S., Nomoto, K., Truran, J. W., & Hashimoto, M. 1997b, Nucl. Phys. A, 621, 499
Ward, R. A., & Fowler, W. A. 1980, ApJ, 238, 266
Weiss, A., & Truran, J. W. 1990, A&A, 238, 178
Wiescher, M., Görres, J., Thielemann, F.-K., & Ritter, H. 1986, A&A, 160, 56
Williams, R. E., Ney, E. P., Sparks, W. M., Starrfield, S. G., Wyckoff, S., & Truran, J. W. 1985, MNRAS, 212, 753
Woodward, C. E., Gehrz, R. D., Jones, T. J., & Lawrence, G. F. 1992, ApJ, 384, 41
Woodward, C. E., Gehrz, R. D., Jones, T. J., Lawrence, G. F., & Skrutskie, M. F. 1997, ApJ, 477, 817
Woodward, C. E., et al. 1995, ApJ, 438, 921
Yungelson, L., Livio, M., & Tutukov, A. 1997, ApJ, 481, 127